AGU ADVANCING EARTH AND SPACE SCIENCES

Earth's Future

RESEARCH ARTICLE
10.1029/2025EF006486

Global Heatwaves Dynamics Under Climate Change Scenarios: Multidimensional Drivers and Cascading Impacts

Oluwafemi E. Adeyeri[1,2], Wen Zhou[3,4], Christopher E. Ndehedehe[5,6], Kazeem A. Ishola[7,8], Patrick Laux[9], Akintomide A. Akinsanola[10], Mame D. B. Dieng[9], and Xuan Wang[2]

[1]ARC Centre of Excellence for the Weather of the 21st Century, Fenner School of Environment and Society, The Australian National University, Canberra, ACT, Australia, [2]Low-Carbon and Climate Impact Research Centre, School of Energy and Environment, City University of Hong Kong, Kowloon, Hong Kong, [3]Key Laboratory of Polar Atmosphere-Ocean-Ice System for Weather and Climate, Ministry of Education and Department of Atmospheric and Oceanic Sciences and Institute of Atmospheric Sciences, Fudan University, Shanghai, China, [4]Key Laboratory for Polar Science of the MNR, Polar Research Institute of China, Shanghai, China, [5]School of Environment and Science, Griffth University, Nathan, QLD, Australia, [6]Australian Rivers Institute, Griffith University, Nathan, QLD, Australia, [7]Department of Geography, Irish Climate Analysis and Research UnitS (ICARUS), Maynooth University, Maynooth, Ireland, [8]National Centre for Geocomputation, Maynooth University, Maynooth, Ireland, [9]Institute for Meteorology and Climate Research Atmospheric Environmental Research, Karlsruhe Institute of Technology, Karlsruhe, Germany, [10]Department of Earth and Environmental Sciences, University of Illinois, Chicago, IL, USA

Abstract Heatwaves are intensifying globally due to climate change. However, the contributions of large-scale atmospheric processes and land-atmosphere interactions to heatwave dynamics and their cascading impacts on water resources and human exposure are not fully understood. This study investigates heatwave frequency (HWF) across 50 global regions, spanning historical (1979–2014) and future periods (2025–2060 and 2065–2100) under SSP 370 (regional rivalry) and SSP 585 (fossil-fuel development) scenarios. Using bias-corrected general circulation model simulations and reconstructed terrestrial water storage (TWS) data, we quantify the contributions of atmospheric processes to HWF modulation and assess the impacts of HWF and temperature changes on water storage deficits using TWS drought severity index (TWS-DSI) and standardized temperature index (STI). We show that Western Central Asia exhibits moisture divergence driven by significant positive thermodynamic effects, which correlates with increased HWF. In West Africa, moisture flux divergence at 1,000 hPa accounts for 45% of HWF variability, while relative humidity at 300 hPa explains 58% of HWF changes in East Asia. HWF and STI strongly influence TWS-DSI, with high STI intensifying TWS deficits. Concurrent high HWF and wet conditions in Western North America are linked to atmospheric blocking and hydrological persistence, highlighting complex illative mechanisms. We project population exposure to HWF to rise tenfold globally by 2100, with regions such as South Asia experiencing over 100% increases due to combined climate and population effects. These findings emphasize the need for tailored adaptation strategies to mitigate heatwave impacts and ensure resilience in a warming world.

Plain Language Summary Heatwaves are becoming more common due to climate change, posing serious challenges for human health, ecosystems, and water resources. This study explores the patterns and causes of heatwaves across 50 regions worldwide, examining both past and future patterns under different climate scenarios. Using advanced climate models and terrestrial water storage data, we investigate how regional factors, such as atmospheric moisture movement, influence heatwaves. We found that regional conditions play a significant role in shaping heatwave patterns. For example, in areas like Western Central Asia and East Asia, moisture loss from the atmosphere is linked to more frequent heatwaves. The study also highlights how heatwaves interact with droughts and temperature extremes. In many regions, extreme heat leads to significant water shortages and worsening drought conditions. However, in some cases, heatwaves can occur without causing drying, showing the diversity of impacts across regions. By 2100, the number of people exposed to heatwaves is expected to increase tenfold, particularly in South Asia and Eastern Africa, due to rising temperatures and population growth. These results highlight the urgent need for tailored solutions to reduce heatwave risks and protect the most vulnerable communities.

Key Points:

- Tropical regions face a projected increase of over 100 heatwave days by 2100, significantly impacting terrestrial water resources
- Heatwave is modulated by land-atmosphere interactions, with regional differences in these processes influencing varied global patterns
- WAF and ARP exemplify contrasting heatwave dynamics driven by monsoonal flows in WAF and subtropical ridges in ARP

Supporting Information:

Supporting Information may be found in the online version of this article.

Correspondence to:

W. Zhou,
wen_zhou@fudan.edu.cn

Citation:

Adeyeri, O. E., Zhou, W., Ndehedehe, C. E., Ishola, K. A., Laux, P., Akinsanola, A. A., et al. (2025). Global heatwaves dynamics under climate change scenarios: Multidimensional Drivers and Cascading Impacts. *Earth's Future*, *13*, e2025EF006486. https://doi.org/10.1029/2025EF006486

Received 23 DEC 2024
Accepted 18 MAY 2025

Author Contributions:

Conceptualization: Oluwafemi E. Adeyeri
Data curation: Oluwafemi E. Adeyeri
Formal analysis: Oluwafemi E. Adeyeri
Funding acquisition: Wen Zhou
Investigation: Oluwafemi E. Adeyeri
Methodology: Oluwafemi E. Adeyeri
Project administration: Wen Zhou
Resources: Oluwafemi E. Adeyeri, Wen Zhou
Software: Oluwafemi E. Adeyeri
Supervision: Wen Zhou, Xuan Wang
Validation: Oluwafemi E. Adeyeri, Wen Zhou, Christopher E. Ndehedehe
Visualization: Oluwafemi E. Adeyeri

Writing – original draft: Oluwafemi E. Adeyeri
Writing – review & editing: Oluwafemi E. Adeyeri, Christopher E. Ndehedehe, Kazeem A. Ishola, Patrick Laux, Akintomide A. Akinsanola, Mame D. B. Dieng

1. Introduction

Heatwaves, characterized by prolonged periods of exceptionally high temperatures, are a growing threat in our changing climate (Adeyeri, Zhou, Ndehedehe, & Wang, 2024; Clarke et al., 2022; Fischer et al., 2021; Perkins-Kirkpatrick & Lewis, 2020; Schär, 2016). Their impacts extend beyond discomfort; they are becoming increasingly dangerous, with significant consequences for human health, ecosystems and socioeconomies. They are associated with heightened human mortality and, morbidity (Xu et al., 2016), as well as severe environmental degradation. As an illustration, the 2010 Russian heatwaves resulted in over 50,000 deaths, more than 500,000 ha of burned land, and US$15 billion of total economic losses (Barriopedro et al., 2011). Similarly, 2003 European heatwaves claimed over 40,000 deaths (Miralles et al., 2014), and heatwaves between 2002 and 2015 caused over 100,000 deaths in Latin America (Kephart et al., 2022). In 2014, Southern Africa experienced significant crop losses and food shortages due to heatwaves, potentially resulting in US$7.4 billion regional economic losses in gross domestic product (IPCC, 2022; Nick et al., 2022). These catastrophic events underscore the increasing frequency and intensity of heatwaves, which are a direct consequence of global climate change. Regardless of future emission trajectories, global mean temperatures will continue to rise, exacerbating this pattern. Climate change, therefore, serves as the primary driver of the increasing prevalence of extreme heat phenomena (Fischer et al., 2021), making understanding and mitigating these impacts critical for societal resilience and safeguarding both human and ecosystem well-being.

Nevertheless, despite the growing threat of extreme heat, our understanding of how climate change affects heatwaves remains limited. This knowledge gap stems from the complexity of the underlying physical processes, including large-scale atmospheric circulation patterns, land-atmosphere interactions, land use changes, energy and moisture feedback mechanisms, and wave activity fluxes (Adeyeri, Zhou, Laux, Wang, et al., 2023; Ha et al., 2022; Wang et al., 2021; Zipper et al., 2019). These processes which contribute to the development and persistence of extreme heat, remain only partially understood. More importantly, these impacts vary worldwide, necessitating uneven distributions of heatwave impacts across the globe. For example, research suggests that atmospheric circulation patterns driving heatwaves often involve abnormally stagnant high-pressure systems (Röthlisberger & Papritz, 2023; Xiao et al., 2024). These systems are linked to hemisphere-wide wave number seven circulation patterns observed in North America, Western Europe, and the Caspian Sea region (Kornhuber et al., 2019), where subsidence and adiabatic warming intensify the heat (Röthlisberger & Papritz, 2023; Yu et al., 2023; Zschenderlein et al., 2019). Concurrently, soil moisture deficits and other land surface processes contribute to increased surface sensible heat fluxes and convective mixing through land-atmosphere feedback, further escalating the severity of heatwaves, especially in mid- and low latitudes (Keune et al., 2022; Röthlisberger & Papritz, 2023; Schumacher et al., 2019). Yet, much of the existing research has been limited to case studies (Vogel et al., 2019), or focuses on single physical processes (Wang et al., 2024; Zschenderlein et al., 2019), leading to inconsistent findings and a fragmented understanding of global heatwaves dynamics (Röthlisberger & Papritz, 2023). Although recent studies have demonstrated the roles of advection over mid-latitude oceans, diabatic heating over tropical and subtropical land, and adiabatic warming near mountains in generating historical heat extremes (Röthlisberger & Papritz, 2023), there remains a pressing need for further analysis to quantify how different physical mechanisms contribute to the projected global increase in heatwaves and to understand how these contributions might evolve in a warming world.

The cascading impacts of persistent heatwaves such as droughts, wildfires, poor air quality, threats to agriculture and biodiversity, and heightened risks of population exposure, pose significant risks to human societies and ecosystems (Adeyeri, Zhou, Laux, Ndehedehe, et al., 2023, Adeyeri, Zhou, Ndehedehe, & Wang, 2024; Brás et al., 2021; Jones et al., 2015; Ndehedehe & Adeyeri, 2024; Tripathy et al., 2023; Vitali et al., 2015). These interconnected effects exacerbate vulnerabilities, particularly in regions that are already struggling with food insecurity, water scarcity, and socio-economic instability. Therefore, understanding the full spectrum of heatwave dynamics, along with their interaction with other environmental variables, becomes essential for informing global strategies aimed at mitigating climate change. This is crucial as it aligns directly with the United Nations Sustainable Development Goals (SDGs), particularly SDG13, which addresses the urgent need to combat climate change and its far-reaching consequences.

This study is motivated by the need to better understand and quantify the contributions of large-scale atmospheric variables to heatwave evolution and dynamics, as well as the broader implications for water resources and human population exposure. By investigating heatwave dynamics across historical (1979–2014) and future (2025–2060

10.1029/2025EF006486

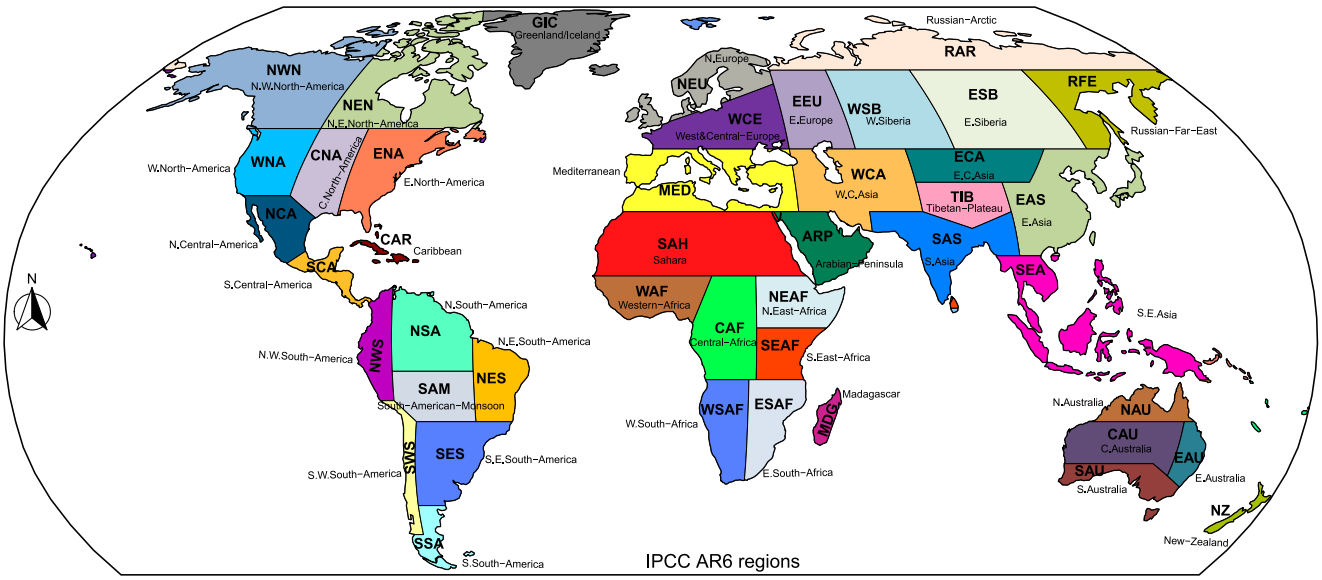

Figure 1. Study area showcasing 50 distinct regions of the Sixth Assessment Report of the Intergovernmental Panel on Climate Change.

and 2065–2100) emission scenarios, we aim to comprehensively analyze how heatwaves are projected to evolve under different climate pathways. Through the use of 10 Coupled Model Intercomparison Project Phase 6 (CMIP6) General Circulation Model (GCM) simulations (Table S1 in Supporting Information S1) under two Shared Socio-economic Pathways (SSPs 370 and 585), we assess the suitability of bias-corrected (BC) GCMs, derived using univariate and multivariate techniques to address the need for a more robust heatwave assessment and the contributions of different atmospheric mechanisms on a global scale. By leveraging the BC GCM outputs, the reconstructed Gravity Recovery and Climate Experiment (GRACE) dataset comprising six separate products (Humphrey & Gudmundsson, 2019), each containing 100 ensemble members, we provide a more comprehensive approach to understanding the interplay between changes in terrestrial water storage (TWS), climate dynamics, and population exposure. Our specific objectives are to (a) quantify the contributions of different atmospheric mechanisms to heatwave frequency (HWF) on a global scale, (b) examine the cascading impact of HWF and the associated temperature anomalies on terrestrial drought severity (TWS deficit), and (c) quantify total population exposure to HWF, considering changes in exposure and their attributions to climate, population dynamics, and their interactions in 50 climate regions (Figure 1) of the Sixth Assessment Report of the Intergovernmental Panel on Climate Change (IPCC AR6) (Iturbide et al., 2021). These findings are crucial for informing effective climate policy, enhancing preparedness, and addressing the vulnerabilities of regions most susceptible to extreme heat.

2. Material and Methods

2.1. Global Reanalysis Products and Terrestrial Water Storage

We leverage the W5E5 v2.0 dataset (Cucchi et al., 2020; Weedon et al., 2014), a merged dataset that combines WATCH Forcing Data (WFDE5)-the Water and Global Change (WATCH) methodology applied to the ECMWF Reanalysis 5 (ERA5) over land area- with the original ERA5 data over the ocean, to bias-correct the climate model simulations and calculate HWF and temperature anomalies. This dataset, designed for bias adjustment in climate model impact assessments, provides global coverage at $0.5° \times 0.5°$ resolution with daily data from 1979 to 2019. Moreover, our study period spans 1979 through 2014 for the historical period. Complementary to this, we utilize Japanese 55 year Reanalysis (JRA55) data (Kobayashi et al., 2015) at $1° \times 1°$ resolution (1,000–300 hPa) for the same period to assess horizontal and vertical moisture flux dynamics and the geopotential height.

We utilize the reconstructed TWS data for 1979–2014 from the GRACE satellite mission to evaluate the cascading impact of HWF and temperature anomalies on terrestrial drought severity. While the GRACE mission offers invaluable monthly estimates of TWS anomalies, its relatively short data span of about 20 years limits our ability to assess long-term hydrological extremes. To overcome this limitation, we leverage the reconstructed GRACE products with a $0.5° \times 0.5°$ grid resolution (Humphrey & Gudmundsson, 2019). These products employ statistical

models to estimate historical climate-induced TWS changes by incorporating daily and monthly meteorological data. They consist of multiple "ensemble members," representing different reconstruction versions based on varied data and models. These variations incorporate perturbed initial conditions from multiple training datasets, parameter perturbations from Markov Chain Monte Carlo sampling, and random residuals to account for uncertainties in the reconstruction process. This ensemble approach of different versions allows us to assess uncertainties and robustly estimate past changes in TWS. Combining two GRACE datasets (Jet Propulsion Laboratory (JPL), and Goddard Space Flight Cente (GSFC)) with three meteorological forcing datasets (ERA5, Global Soil Wetness Project Phase 3 (GSWP3), Multi-Source Weighted-Ensemble Precipitation (MSWEP)), each containing 100 ensemble members, we create one single, robust estimate of the reconstructed TWS for the analysis.

2.2. Global Climate Model and Total Population Data

Our analysis of future heatwave changes employs a ten-model ensemble from CMIP6, including, CMCC-ESM2, CNRM-CM6-1, INM-CM5-0, IPSL-CM6A-LR, KACE-1-0-G, MIROC6, MPI-ESM-1-2HR, MPI-ESM-1-LR, MRI-ESM2-0, UKESM1-0-LL and their multimodel ensemble mean (see Table S1 in Supporting Information S1 for the fullnames and resolutions), selected using the ClimWIP method (Merrifield et al., 2023) to minimize model dependence. This method groups models based on long-term climate similarities, effectively averaging internal variability and parameter uncertainty while preserving distinctions between model structures. We consider SSP 370 (regional rivalry) and SSP 585 (fossil-fuel development) scenarios (7.0 and 8.5 W m^{-2} radiative forcing, respectively) for the near future (2025–2060) and far future (2065–2100).

To assess the exposure of the total human population (i.e., combined rural and urban population) to HWF, we utilize historical annual population data from the Inter-Sectoral Impact Model Intercomparison Project (ISIMIP) protocol, ISIMIP2b, available at an approximate spatial resolution of 0.083°, and future population projections from the NASA Socio-economic Data and Applications Center at 0.125° resolution. These datasets, provided under various SSP scenarios, leverage a gravity-type model to parameterize spatial patterns of change for each SSP, enabling robust scenario-based demographic projections (Jones & O'Neill, 2016). Future population data is available at 10 year intervals; therefore, we calculate the mean population for each future period to assess total population exposure to heatwaves. We regrid all datasets to a standard $2° \times 2°$ grid to harmonize the varying resolutions of the GCMs used in this study, thereby reducing the scale gap effect (Adeyeri, Zhou, et al., 2022) and ensuring consistency across datasets without compromising the robustness of our analysis. This approach aligns with established practices in climate modeling (Adeliyi et al., 2025; Adeyeri, Zhou, et al., 2022; Akinsanola et al., 2025; Ndehedehe, Adeyeri, et al., 2023; Taguela et al., 2025). Conservative variables like precipitation, population, specific humidity, and geopotential heights undergo conservative remapping, while non-conservative variables such as GRACE, temperature, and zonal and meridional winds are bilinearly remapped (Schulzweida, 2022).

2.3. Bias Correction of Climate Models

While climate models provide valuable projections of future heatwaves under different scenarios, discrepancies between model simulations and observations raise concerns about their accuracy. These discrepancies from resolutions, variations in model components, and land surface schemes (Adeyeri et al., 2020; Cannon et al., 2015; Dieng et al., 2022; Laux et al., 2021) necessitate BC to enhance the reliability of climate change projections (Usman et al., 2022). This crucial step has been overlooked in many heatwave studies using GCM simulations (Adeyeri, Zhou, Ndehedehe, & Wang, 2024; Ha et al., 2022; Jones et al., 2015; Ullah et al., 2023; Wang et al., 2023), potentially compromising the validity of their findings. To correct biases in our CMIP6 model simulations, we use univariate quantile delta mapping (QDM) and a multivariate BC method employing an N-dimensional probability density function transform (MBCN) (Cannon, 2018). The univariate method assumes an accurate model projection of historical and future quantiles (Adeyeri et al., 2020; Déqué et al., 2007). The multivariate method differs by preserving changes in simulated quantiles while updating marginal distributions via quantile mapping and adjusting the joint multivariate dependence of multiple variables at once (Cannon, 2018), while reassigning all properties of the observed distribution to the climate simulations (Adeyeri, Zhou, Ndehedehe, Wang, & Ishola, et al., 2024). To preserve the joint multivariate dependence relevant to heatwaves, we use daily near-surface relative and specific humidity, precipitation, surface and sea level pressure, surface downwelling longwave and shortwave radiation, near-surface wind speed, and daily maximum, minimum, and average near-surface air temperature from the reference dataset to bias-correct the CMIP6 models. We provide details of this method in appendices Appendix A.

2.4. Heatwave and Standardized Temperature Index Derivation

Among various heatwave characteristics, we focus on the number of days contributing to heatwaves as identified by the heatwave number and defined by excess heat factor (EHF), hereafter called HWF. Excess heat factor identifies periods with three or more consecutive days exceeding a specific threshold (Adeyeri, Zhou, Ndehedehe, & Wang, 2024; Perkins-Kirkpatrick & Lewis, 2020). This threshold is calculated using a 3 day temperature average, compared against both the 90th percentile of historical summer temperatures and the recent 30 day temperatures (Perkins et al., 2015). We select the EHF to define HWF because it considers the intensity and the duration of temperature anomalies. This approach provides a reliable metric for analyzing heatwaves (Nairn et al., 2018), while its standardized methodology allows for direct comparisons across different regions.

To convert the continuous EHF into a discrete HWF variable suitable for our subsequent analyses, we employ a three-step transformation.

(a) We consider only those days where EHF is positive (i.e., EHF > 0), (b) A heatwave event is defined as any period comprising three or more consecutive days satisfying the EHF > 0 criterion, and (c) Within each chosen temporal interval, HWF is calculated by summing the total number of heatwave days—those with EHF > 0. This approach produces a continuous count metric of heatwave occurrences.

The EHF is calculated as follows:

$$EHF = EHI_{sig} * \max[EHI_{acc}, 1] \tag{1}$$

where $EHI_{sig} = \frac{[T_k + T_{k-1} + T_{k-2}]}{3} - T_{90}$, $EHI_{acc} = \frac{[T_k + T_{k-1} + T_{k-2}]}{3} - \frac{[T_{k-3} + \ldots + T_{k-32}]}{30}$ and $\mathrm{T} = \frac{[T_{\max} + T_{\min}]}{2}$. Where T_{90} is the climatological 90th percentile temperature during the base period (1982–2010), T, $T_{\min}$, $T_{\max}$, and T_k denote the daily mean air, minimum, maximum, and kth day daily mean temperatures, respectively. We calculate T90 for each day of the year during the base period using a 15 day centered window and smooth it with a Savitzky-Golay third-order polynomial filter (Adeyeri, Zhou, Ndehedehe, & Wang, 2024). This window-based approach allows us to capture the full range of variations in heatwave metrics throughout the year, regardless of seasonality. EHI_{acc} measures the current 3 day temperature variance relative to the prior month's average, highlighting recent temperature fluctuations; $EHI_{sig,}$ on the other hand, quantifies the divergence of the current 3 day period's temperature from the climatological relative threshold.

We calculate the difference between (a) the far future and the historical period, (b) the near future and the historical period, and (c) the far future and the near future to determine the HWF climate change signal (Adeyeri, Zhou, et al., 2022).

The standardized temperature index (STI), analogous to the standard precipitation index (SPI), represents the probability of a given temperature relative to a longer-term baseline. Unlike SPI, STI does not accumulate temperature but uses daily values. Positive and negative STI values indicate temperatures above and below the long-term median, respectively, allowing identification of unusually hot or cold periods. We calculate the STI by fitting a parametric normal distribution to daily temperatures based on the cumulative distribution $G(x)$ over the extended summer period considered for this study (Zscheischler et al., 2014).

$$G(x) = \frac{1}{\sigma\sqrt{2\pi}} \int_{-\infty}^{x} exp\left[-\frac{(x-\mu)^2}{2\sigma^2}\right] dx \tag{2}$$

$$STI = \varphi^{-1}(q)$$

where x, μ, and σ represent the temperature time series, mean, and standard deviation, respectively; q is the cumulative probability, and φ is the standard normal distribution.

2.5. Moisture Flux Dynamics, Teleconnection, and Their Relative Contributions to Heatwave Modulation

Moisture flux divergence is calculated as the divergence of the moisture flux vector, which combines the horizontal and vertical components of moisture flow. Positive divergence indicates a net moisture loss from the region, whereas negative divergence signifies a net gain (convergence). Using the specific humidity (q),

horizontal winds (v), and surface pressure (P_s), we derive the horizontal moisture flux divergence ($\nabla.Q$) , which is given as:

$$\nabla.Q = \nabla.\frac{1}{g}\int_0^{P_s} qvdp \tag{3}$$

The vertically integrated moisture flux convergence (VIMFC) or vertically integrated moisture flux divergence (VIMFD or negative VIMFC), from 300 hPa to 1,000 hPa is given as:

$$VIMFC = -\frac{1}{g}\int_{300\ hPa}^{1000\ hPa} \nabla.\left(q\vec{V}\right)dp = -\frac{1}{Sg}\int\int qVdldp \tag{4}$$

where s is the size of the integration region, V is the wind vector, and dl is the grid length along the latitude and longitude. The relative contribution of the dynamic and thermodynamic processes associated with moisture transport is quantified by expanding the right-hand side of Equation 4, and this is given as:

$$\frac{1}{g}\int\int -qVdldp = \frac{1}{g}\int\int -\overline{q}\overline{V}dldp + \frac{1}{g}\int\int -q'\overline{V}dldp + \frac{1}{g}\int\int -\overline{q}V'dldp + \frac{1}{g}\int\int -q'V'dldp \tag{5}$$

The average term is denoted by the first term on the right hand, which is constant throughout the study period. The moisture flow anomalies brought on by the thermodynamical and dynamical processes are the second and third terms, respectively. The last term is the minor deviations from the climatology, which can be neglected. Integrated vapor transport (IVT) is used to understand the dynamics of water vapor movement in or out of a particular domain. Integrated vapor transport is defined as (Adeyeri, Zhou, Ndehedehe, Wang, & Ishola, et al., 2024):

$$IVT = \frac{1}{g}\int_{300\ hPa}^{1000\ hPa} q\vec{V}dp \tag{6}$$

Vapor transport (VT) is given as:

$$VT = q\vec{V} \tag{7}$$

$\overline{q}$ and $\overline{V}$ are the climatology of specific humidity and wind. q' and V' are the deviations of q and V from the climatology, and g is the gravitational constant.

We use Empirical Orthogonal Teleconnections (EOTs), a regression-based method (Acppelhans et al., 2015), to identify and analyze climate variability patterns across different spatial locations. Empirical Orthogonal Teleconnections decompose data into spatial patterns (empirical orthogonal functions, EOFs) and associated time series (principal component time series). EOFs represent the spatial structure of the variability, while the principal component time series captures the temporal evolution of the patterns. In comparison, EOFs detect prominent patterns of variability in the data, whereas EOTs employ these patterns to investigate the teleconnections between various parts of the Earth's climate system. We utilize the EOTs to understand the teleconnection between HWF and the VIMFD components, that is, the dynamic and thermodynamic terms and IVT.

Recognizing the inherent interconnectedness of these variables, we further explore the relative contributions of these dynamic and thermodynamic variables to HWF response. While various methodologies exist for assessing these relationships, permutation importance, a technique leveraging the strengths of random forest algorithms (Adeyeri, Zhou, et al., 2022; Breiman, 2001), offers several advantages and is therefore widely employed. However, the traditional approach to permutation importance from random forest is not ideal for highly correlated variables. This method cannot differentiate between the conditional (specific context-dependent) and marginal (overall) influences of each variable (Adeyeri, Folorunsho, et al., 2024). Therefore, we employ the conditional permutation importance (CPI) method (Adeyeri et al., 2022; Strobl et al., 2008) to address this challenge and better understand the contributions of the multivariate drivers on HWF. We provide details of this method in appendices Appendix B.

2.6. Deriving Terrestrial Water Storage Drought Severity and Standardized Temperature Index

Heatwaves have cascading impacts on TWS drought conditions. Moreover, changes in TWS can also influence heatwaves. Leveraging the reconstructed TWS, we calculate the terrestrial drought condition using the TWS drought severity index (DSI) (Zhao et al., 2017).

$$TWS - DSI_{i,j} = \frac{\left(TWS_{i,j} - \overline{TWS_j}\right)}{\mu_j}, \tag{8}$$

where $TWS_{i,j}$ is the TWS anomalies at year i and month j, and $\overline{TWS_j}$ and μ_j are the mean and standard deviation of TWS anomalies at month j.

Following the multivariate standardized drought classification (Adeyeri, Zhou, Laux, Ndehedehe, et al., 2023), we classify TWS–DSI ≥2.00 as extremely wet; between 1.50 and 1.99 as severely wet; from 1.00 to 1.49 as moderately wet; from 0.00 to 0.99 as mildly wet; between −0.99 and 0.00 as mild drought; from −1.49 to −1.00 as moderate drought; between −1.99 and −1.50 as severe drought, and ≤ −2.00 as extreme drought.

2.7. Total Population Exposure to Heatwave

To calculate total population (i.e., combined rural and urban population) exposure to HWF, we multiply the total population by HWF at each grid point for reference and future periods (Jones et al., 2015), that is, $E = \mathrm{P} * \mathrm{HWF}$. We then compute the 35 year mean exposure under various climate change scenarios to understand the total change in population exposure to HWF. We break down the total change in population exposure to heatwaves into three components: climate effects, population effects, and their interactions. The climate effect on total population exposure represents the climate influence on exposure when transitioning from historical to future scenarios, with the population held constant at the historical level. On the other hand, the population effect on total population exposure measures the impact of population projections on exposure while the climate remains constant at the historical level. Finally, the interaction effect captures the simultaneous exposure to climate and population dynamics.

The total change in exposure (ΔE) is given as:

$$\Delta \mathrm{E} = P_h \Delta C + C_h \Delta P + \Delta C \Delta P, \tag{9}$$

where P_h and C_h denote the historical population and HWF, respectively, while ΔP and ΔC represent the change in population and HWF from the historical to the future period. In this formulation, $P_h \Delta C$, $C_h \Delta P$ and $\Delta C \Delta P$ correspond to the climate, population, and interaction effects, respectively.

2.8. Partial Correlation of Large-Scale Variables With Heatwave

The strength of the relationship between two variables is typically measured by their degree of association between them. However, partial correlation is used when the influence of a third variable or multiple other variables needs to be accounted for. This method assesses the correlation between two variables while controlling for the influence of other variables, thus providing a clearer picture of the primary relationship in question (Adeyeri, Zhou, et al., 2022, Adeyeri, Folorunsho, et al., 2024). Given the numerous regional factors influencing HWF, we employ partial correlation to examine HWF relationship with various regional climatic drivers.

The partial correlation is given as follows:

$$\rho KMB = \frac{\rho KM - \rho KB \rho MB}{\sqrt{(1 - \rho^2 KB) * (1 - \rho^2 MB)}} \tag{10}$$

For a set of n controlled climate forcing variables, B is

$$B = \{B_1, B_2, .., B_n\}$$

We apply the Student's *t*-test to check the statistical significance of the partial correlations at the 95% confidence level. All our analyses are based on the extended summer seasons in the northern and southern hemispheres, that is, from May to September and November to March, respectively.

3. Results

3.1. Performance and Bias Correcting GCMs for Driving Variables of Heatwave

Biases in climate models can lead to inaccurate projections of future climate conditions. Therefore, it is crucial to quantify and correct these biases before utilizing climate models for impact studies. Figures S1 and S2 in Supporting Information S1 show varying biases in the climatology of the uncorrected CMIP6 models' temperature and relative humidity (RH), respectively. For example, CNRM-CM6-1, IPSL-CM6A-LR, and UKESM1-0-LL record cold biases for most areas, while MIROC6 exhibits hot biases. The cold and warm biases vary from −20°C to 16°C. However, most North America and Central Asia areas witness wet biases for all models, while the tropical regions mostly witness dry biases in RH. IPSL-CM6A-LR has the lowest biases, particularly over Africa. All models' dry and wet biases range between −44% and 44%. After identifying the different levels of biases, we correct them using QDM and MBCN techniques. Figures S3 and S4 in Supporting Information S1 illustrate the CMIP6 temperature climatology distribution after BC with MBCN and QDM, respectively, revealing notable reductions in biases across all CMIP6 models, although some residual biases remain. Figures S5 and S6 in Supporting Information S1 show the BC for RH using MBCN and QDM, respectively, mirroring the improvements highlighted in temperature. Nevertheless, the CMCC-ESM2 model exhibits more dry biases than others.

Given that temperature and RH influence the perception of heatwaves as human thermal stress (Adeyeri, Zhou, Laux, Wang, et al., 2023), we examine the CMIP6 models' ability to establish the mutual dependence between these two variables. Figure S7 in Supporting Information S1 shows the dependency between temperature and RH for uncorrected CMIP6 models, with values close to zero indicating an accurate dependency. Moreover, the values for all uncorrected models range between 0.4 and 1.6, with the tropics showing higher values (>1), indicating that the uncorrected CMIP6 models struggle to maintain the necessary dependency. Conversely, the MBCN-corrected models preserve this dependency, with values close to zero across all continents (Figure S8 in Supporting Information S1). In contrast, the QDM-corrected models fail to maintain this dependency on all continents (Figure S9 in Supporting Information S1). Additionally, Figure S10 in Supporting Information S1 shows that the HWF root mean square error (RMSE) ranges from 0 to 20 days in the uncorrected CMIP6 model, while the MBCN-corrected models exhibit an RMSE ranging from 0 to 1 day in most areas across all models. Furthermore, the validation of regional HWF in Figure S11 in Supporting Information S1 complements these results. Ultimately, the MBCN approach successfully corrects model biases while preserving the variables' dependency structures.

3.2. Heatwave and the Influence of Large-Scale Atmospheric Processes

This section examines the interaction between HWF and several large-scale processes. We observe unique regional fingerprints, underscoring the critical need for region-specific assessments over a one-size-fits-all approach.

Figure 2 illustrates the spatial relationships between HWF and key modulating factors, including moisture flux divergence (MFD) and RH at different tropospheric levels, as well as precipitation, air temperature, TWS, VIMFD, and its dynamic and thermodynamic components. These relationships, statistically significant at the 95% confidence level, demonstrate the spatially varying influence of these factors across the atmospheric column and different regions. For instance, in the lower troposphere (Figure 2a), MFD positively correlates with HWF in Northern Central America (NCA), Southeastern South America (SES), Western Africa (WAF), the Sahara (SAH), and Northern Europe (NEU). Conversely, negative correlations appear in Western and Central Europe (WCE), Eastern Europe (EEU), the South America Monsoon (SAM), Central Australia (CAU), and the Arabian Peninsula (ARP). Moving to the mid-troposphere (Figure 2b), the influence of MFD on HWF essentially reverses in these regions, highlighting the distinct roles of the lower and mid-troposphere in shaping heatwave dynamics and moisture transport. In the upper troposphere (Figure 2c), the positive influence of MFD becomes more widespread, particularly across Africa, South America, Asia, the Arabian Peninsula, and Australia.

10.1029/2025EF006486

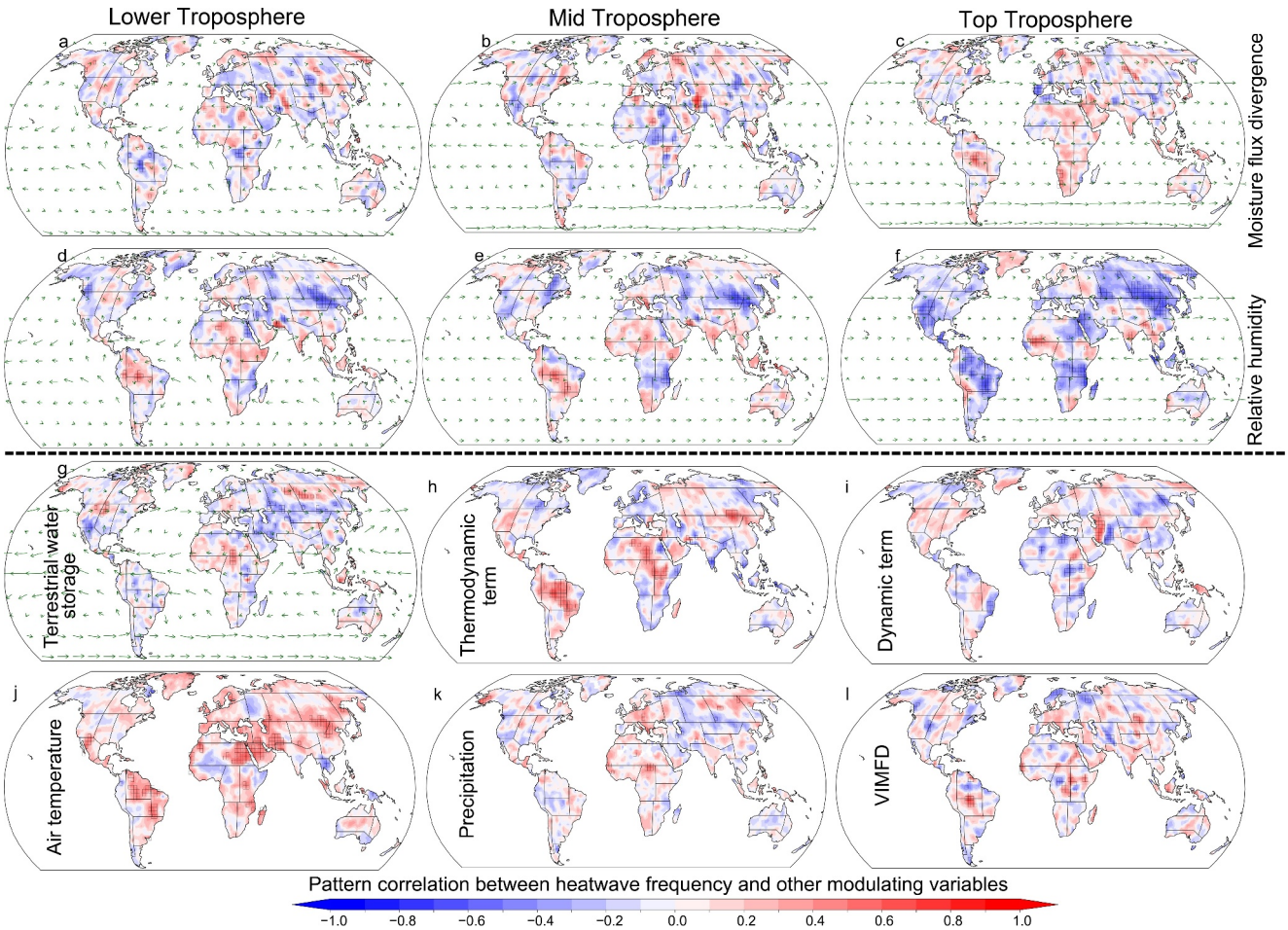

Figure 2. Pattern correlation between heatwave frequency and various atmospheric and terrestrial variables for (a) Moisture flux divergence at the lower troposphere (1,000 hPa, background), with vectors representing wind at 1,000 hPa, (b) Moisture flux divergence at the mid-troposphere (500 hPa, background), with vectors representing wind at 500 hPa, (c) Moisture flux divergence at the upper troposphere (300 hPa, background), with vectors representing wind at 300 hPa, (d) relative humidity (RH) at the lower troposphere (background), with vectors representing Vapor transport (VT) at 1,000 hPa, (e) RH at the mid-troposphere (500 hpa, background), with vectors representing VT at 500 hPa, (f) RH at the upper troposphere (300 hpa, background), with vectors representing VT at 300 hPa, (g) Terrestrial water storage (background), with vectors representing vertically integrated vapor transport from 1,000 hPa to 300 hPa, (h) Thermodynamic term of vertically integrated moisture flux divergence, (i) Dynamic term of the vertically integrated moisture flux divergence, (j) Air temperature, (k) Precipitation, and (l) Vertically integrated moisture flux divergence from the upper to lower troposphere. Boxes represent significant correlations at a 95% confidence level.

In regions like NEU, NCA, SES, East Siberia (ESB), and East Central Asia (ECA), the positive influence of MFD aligns with a negative HWF-RH relationship near the surface (Figures 2d and 2f), signifying typical dry heatwave conditions, where drier surface conditions (Figure 2g) contribute to increased air temperature (Figure 2j) via land-atmosphere feedback. In this context, the statistical association is consistent with established feedback hypotheses —that drier conditions amplify surface heating—but we note that our methods infer rather than directly demonstrate these feedback processes.

Focusing on two contrasting regions, WAF and ARP, these regions exemplify distinct heatwave dynamics driven by moisture transport and atmospheric circulation. In WAF (Figure 2a), lower-tropospheric MFD correlates positively with HWF, driven by monsoon winds and the Saharan High (Figure A1). These processes enhance southward moisture transfer from the Mediterranean, intensifying heatwaves in the Sahara despite moisture inflow from the Atlantic. Conversely, in ARP (Figure 2a), lower-level VT offsets subsidence effects from the high-pressure system (Figure A1), reducing HWF as MFD increases. This contrast highlights how regional circulation patterns—monsoonal flows in WAF versus subtropical ridges in ARP—dictate heatwave mechanisms. Further, the decomposition of VIMFD reveals the individual contributions of dynamic and thermodynamic effects to HWF (Figures 2h, 2i, and 2l). Significant positive VIMFD correlations over the SAM and ECA coincide

10.1029/2025EF006486

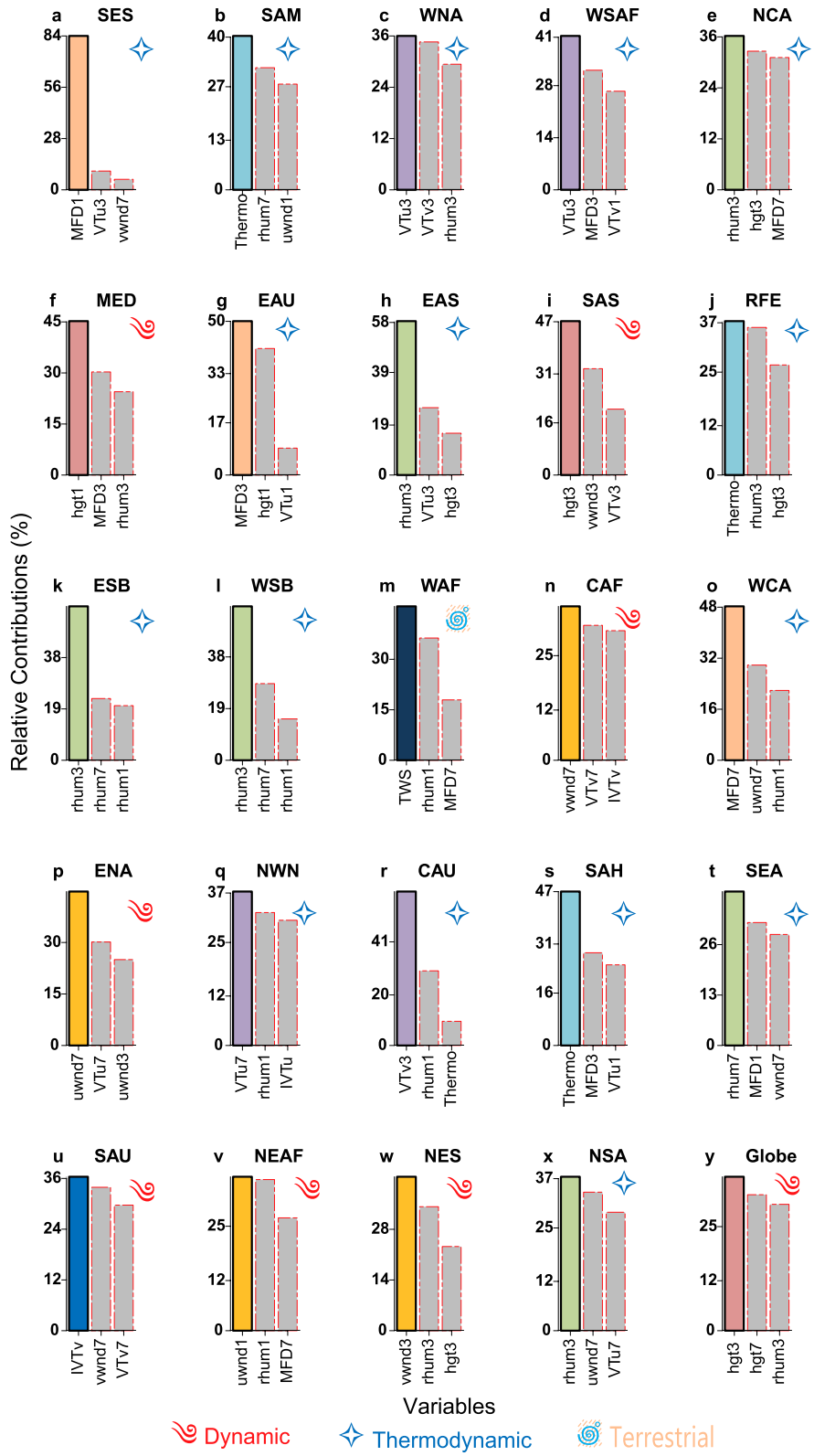

Figure 3.

with regions exhibiting significant positive thermodynamic responses. However, in West Central Asia, significant positive dynamic effects—linked to moisture divergence—are associated with a tendency toward more frequent heatwaves (Figure A1a). While these decomposed associations support the notion that both dynamic and thermodynamic processes contribute to conditions favorable for feedback mechanisms, we acknowledge that the evidence presented remains inferential.

Furthermore, high HWF is mitigated in regions like WAF and Central Africa (CAF), there is robust lower tropospheric moisture flow from the Atlantic Ocean into the interiors, driven by monsoon winds, the monsoon trough over the Sahara (SAH), and a weak ridge across the Mediterranean (MED) (Figure A1, and Figure 2). In the mid-troposphere, the Saharan High and the African Easterly Jet (AEJ) synergize to enhance southward moisture transfer from the Mediterranean into WAF and CAF (Figures A1b and A1d, and Figures 2b and 2g), increasing HWF over the SAH. Thus, the relationship between these variables considerably influences HWF in WAF, SAH, and CAF. Orography (Figure A1c) and IVT (Figure A1d) also influence temperature distribution and HWF. For example, the interaction between the Himalayas in SAS and TIB, moisture transport, and monsoon winds play a key role in modifying summer heatwaves over India, especially on the windward side of the mountains. Despite the moisture brought by monsoon winds (Figures A1a and A1d), the windward side of the Himalayas (Figure A1c) experiences high temperatures (Figure A1b) and frequent heatwaves (Figure A1a). Contrary to the effect of moisture abundance in mitigating frequent heatwaves in WAF and CAF despite having similar temperatures as SAS, the unique climatic conditions in SAS mean that even with moisture, intense heat can still lead to significant heatwave events, particularly under clear skies and high solar radiation.

However, MDG and SEAF experience higher HWF (Figure A1a) compared to WAF and CAF due to the absence of features like the low-level trough and mid-level jet (Figures A1a and A1b), which are critical for enhancing moisture transport inland (Figure A1d). In Northern Australia (NAU), easterly winds from the Western Pacific Ocean transport moisture (Figures A1a and A1d). However, low tropospheric (Figure A1a) and mid-tropospheric (Figure A1b) pressure centers push the moisture northwards, enabling moisture recycling into Southern East Asia (SEA) from NAU. Consequently, NAU has high HWF, while SEA experiences relatively low HWF. As exemplified above, each region's unique geographical and orographic influences and moisture transport mechanisms substantially impact HWF.

3.3. Regional Contributions of Large-Scale Processes to Heatwave Modulation

Having established that each region's unique characteristics greatly impact HWF, assessing the dependency of HWF on different large-scale processes across distinct climate domains becomes necessary. Figures 3a–3y demonstrate that the relative contributions of large-scale atmospheric and terrestrial variables to HWF vary across different regions.

In Southeastern South America (SES), moisture flux divergence at 1,000 hPa contributes 84% to HWF modulation (Figure 3a), while zonal VT at 300 hPa and meridional winds at 700 hPa each account for less than 8%. In

Figure 3. Relative contribution of large-scale atmospheric and terrestrial variables to heatwave frequency modulation in various regions (a) Southeast South America, (b) South American Monsoon, (c) Western North America, (d) Western Southern Africa, (e) West and Central Europe, (f) Mediterranean, (g) Eastern Australia, (h) East Asia, (i) South Asia, (j) Russian Far-East, (k) Eastern Siberia, (l) Western Siberia, (m) West Africa, (n) Central Africa, (o) West Central Asia, (p) Eastern North America, (q) Northwest North America, (r) Central Australia, (s) Sahara, (t) Eastern North America, (u) South Australia, (v) Northern East Africa, (w) Northeast South America, (x) Northern South America, and (y) Globe. Uwnd and vwnd mean zonal and meridional wind; Thermo means the thermodynamic term of vertically integrated moisture flux divergence; rhum is the relative humidity; VTu and VTv are the zonal and meridional vapor transports; MFD is the moisture flux divergence; IVTu and IVTv are the zonal and meridional vertically integrated moisture flux transport; Dyna is the dynamic term of the vertically integrated moisture flux divergence; terrestrial water storage (TWS) is the TWS; hgt is the geopotential height; 3, 7, and 1 indicate 300, 700, and 1,000 hPa, respectively. The bold bar represents the variable with the highest contribution. Some variables, like moisture flux divergence and integrated vapor transport, have both dynamic and thermodynamic components. However, for categorization purposes, if the focus is on the motion (e.g., wind-driven processes), they lean toward being dynamic. If the focus is on the moisture and energy content, they lean toward being thermodynamic. The dynamic variables are primarily associated with atmospheric motion, wind patterns, or pressure-driven processes. They consist the uwnd, vwnd, hgt, MFD. The thermodynamic variables are associated with moisture content, energy, or phase changes. They include rhum, IVTu, IVTv, VTu, VTv (moisture movement, even if wind contributes), and Thermo. The terrestrial variable is TWS.

10.1029/2025EF006486

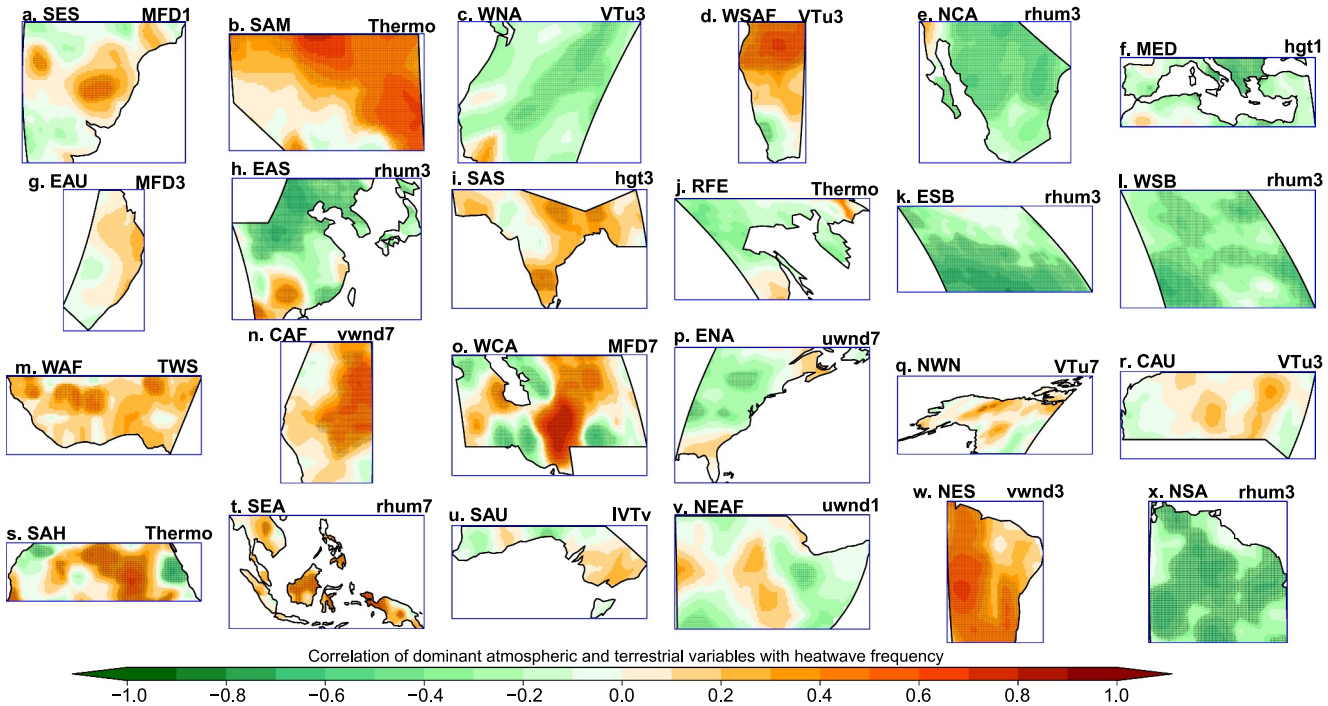

Figure 4. Correlation between heatwave frequency and the principal regional large-scale atmospheric and terrestrial variables modulating it. Boxes represent significant correlations at a 95% confidence level.

the South American Monsoon region (SAM), the thermodynamic term of vertically integrated moisture flux convergence, RH at 700 hPa, and zonal winds at 1,000 hPa collectively account for 41%, 32%, and 27% of HWF modulation, respectively (Figure 3b). In East Asia (EAS), RH at 300 hPa explains 58% of HWF variation (Figure 3h), while in West Africa (WAF), TWS contributes 45% (Figure 3m). Globally, geopotential height at 1,000 and 700 hPa, and RH at 300 hPa, primarily drive HWF (Figure 3y). Thermodynamic processes dominate HWF modulation in regions such as Western North America (WNA), Western South Africa (WSAF), SAM, Eastern Australia (EAU), West Siberia (WSB), Northern Central America (NCA), Russian Far-East (RFE), Western Central Asia (WCA), and Central Australia (CAU). In contrast, dynamic processes dominate in Eastern North America (ENA), Central Africa (CAF), South Asia (SAS), Norther East Africa (NEAF) and Southern East Asia (SEA) regions. Despite the proximity of CAF to WAF, terrestrial process dominate WAF, while dynamic processes dominate HWF modulation in CAF, reflecting the complexities associated with HWF drivers.

Furthermore, we examine the partial correlation between HWF and the principal regional large-scale atmospheric and terrestrial variables modulating it (Figures 4a–4x). In Southeastern South America (SES, Figure 4a), the 1,000 hPa moisture flux divergence (MFD1) shows mixed correlations with HWF, suggesting competing effects of drying and moisture convergence. Positive correlation coefficients indicate that increased subsidence may lead to increased divergence (positive MFD1), potentially reducing surface evaporation and local moisture availability, and thus contributing to higher temperatures and increased HWF (Figure A1). Conversely, negative correlations suggest a mitigating influence from Atlantic moisture inflow, supporting evaporative cooling. Subtropical high-pressure systems frequently dominate the SES, advecting warm, dry air inland (Figure A1a). This advection, combined with potential anthropogenic factors such as agricultural expansion and deforestation, may amplify regional heating through reduced evapotranspiration. In the South American Monsoon region (SAM, Figure 4b) region, a positive correlation exists between the thermodynamic term (Thermo) and HWF, suggesting a link between heat-driven atmospheric instability and HWF during monsoon breaks. Inland areas, less influenced by oceanic effects, may be particularly susceptible to prolonged heating due to suppressed moisture conditions.

Figure 4c shows that enhanced upper-level zonal VT (VTu3) in Western North America (WNA) can offset these warming influences of the increased subsidence reinforced by existing high-pressure systems (Figure A1a).

10.1029/2025EF006486

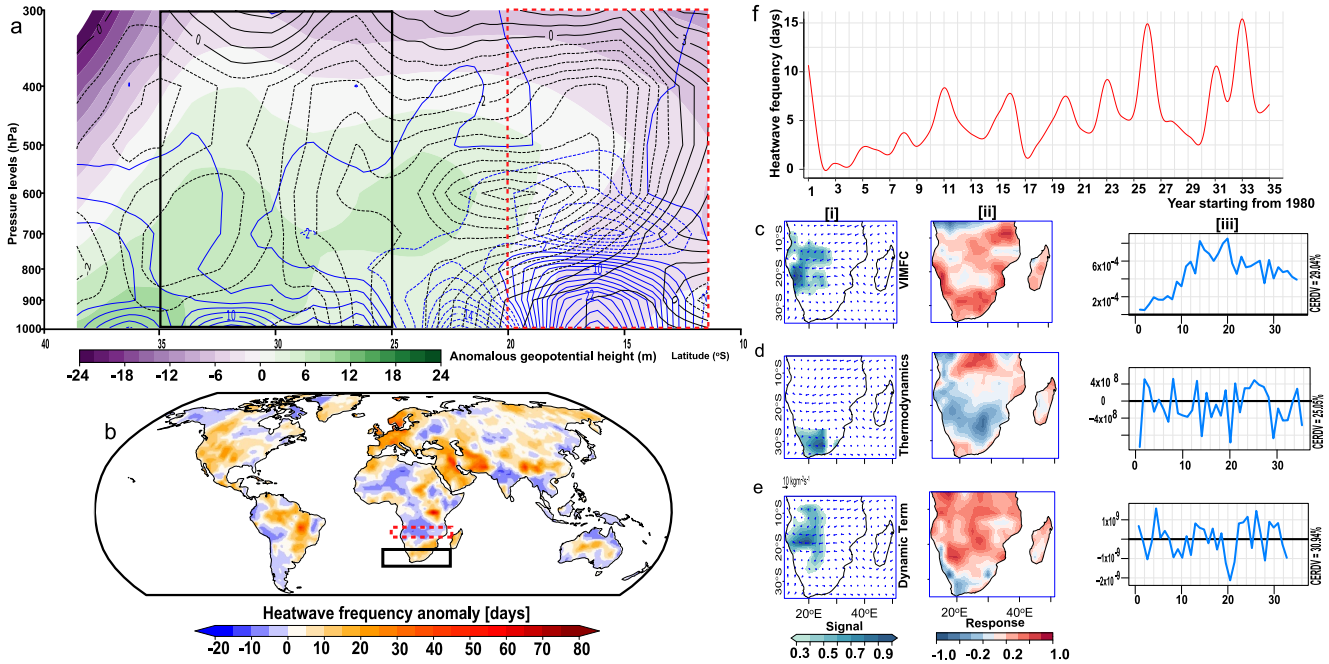

Figure 5. A case study of Western and Eastern South Africa Heatwave Dynamics. (a) Synoptic conditions during the 2014 heatwave, showing geopotential height (background), moisture flux convergence (blue contours), and relative humidity (black contours), (b) Anomalous heatwave frequency (HWF) in 2014, (c)–(e) Teleconnection analysis of HWF with (i) Integrated vapor transport from 1,000 to 300 hPa and their associated teleconnection patterns, (ii) HWF signals, and (iii) Cumulative Explained Response Domain Variance (CERDV), and (f) Temporal evolution of HWF (days) from 1980 to 2014.

Conversely, Western South Africa (WSAF, Figure 4d) shows that enhanced (VTu3) positively correlates with HWF. This transport reinforces ridge-building high-pressure systems, intensifying subsidence and reducing cloud cover. Coastal regions benefit from the cooling influence of the Benguela Current, while inland semi-arid areas are more sensitive to moisture variability and subsidence effects linked to the South Atlantic High (Figure A1a). Geopotential height at 1,000 hPa (hgt1) exhibits a strong positive correlation with HWF in the Mediterranean (MED), driven by the dominance of stationary high-pressure systems (Figure A1). These ridges enhance subsidence, clear-sky conditions, and solar heating, particularly over inland areas. Coastal regions, though adjacent to the Mediterranean Sea, are less affected by moisture moderation during heatwaves due to the persistent anticyclonic patterns. Moisture flux divergence at 300 hPa (MFD3, Figure 4g) demonstrates mixed correlations with HWF. Positive correlations are linked to increased divergence aloft (Figure A1b), which supports subsidence and drying, while negative correlations reflect the mitigating influence of convergence, potentially enhancing cloud formation and precipitation. Proximity to the Tasman Sea and the Coral Sea provides moisture for EAU coastal regions, whereas inland areas are dominated by the subtropical ridge, which reinforces dry conditions during heatwaves. Relative humidity at 300 hPa (rhum3, Figure 4h) shows mixed correlations in East Asia (EAS), reflecting the dual role of upper-level moisture in heatwave dynamics. Positive correlations occur where enhanced humidity supports latent heat release during convection, while negative correlations dominate under subsidence, which suppresses rainfall and amplifies heat, as evidenced in ESB, WSB, NSA, and NCA.

Furthermore, Figure 4i shows that geopotential height at 300 hPa (hgt3) positively correlates with HWF in South Asia (SAS), where upper-level ridges suppress moisture inflow and enhance subsidence warming. In WAF (Figure 4m), TWS positively correlates with HWF, highlighting the paradoxical role of soil moisture in amplifying surface heat retention. These regional variations in dominant large-scale processes highlight the complex interactions of meteorological phenomena influencing HWF. Therefore, understanding these regional mechanisms is crucial for assessing heatwave risks in a regional context.

3.4. Regional Differences in the Southern Africa Zones During the 2014 Heatwaves

Building on the analysis of large-scale processes influencing HWF across different climate regions, examining how these mechanisms operate at regional scales is important. Southern Africa's experience during the 2014

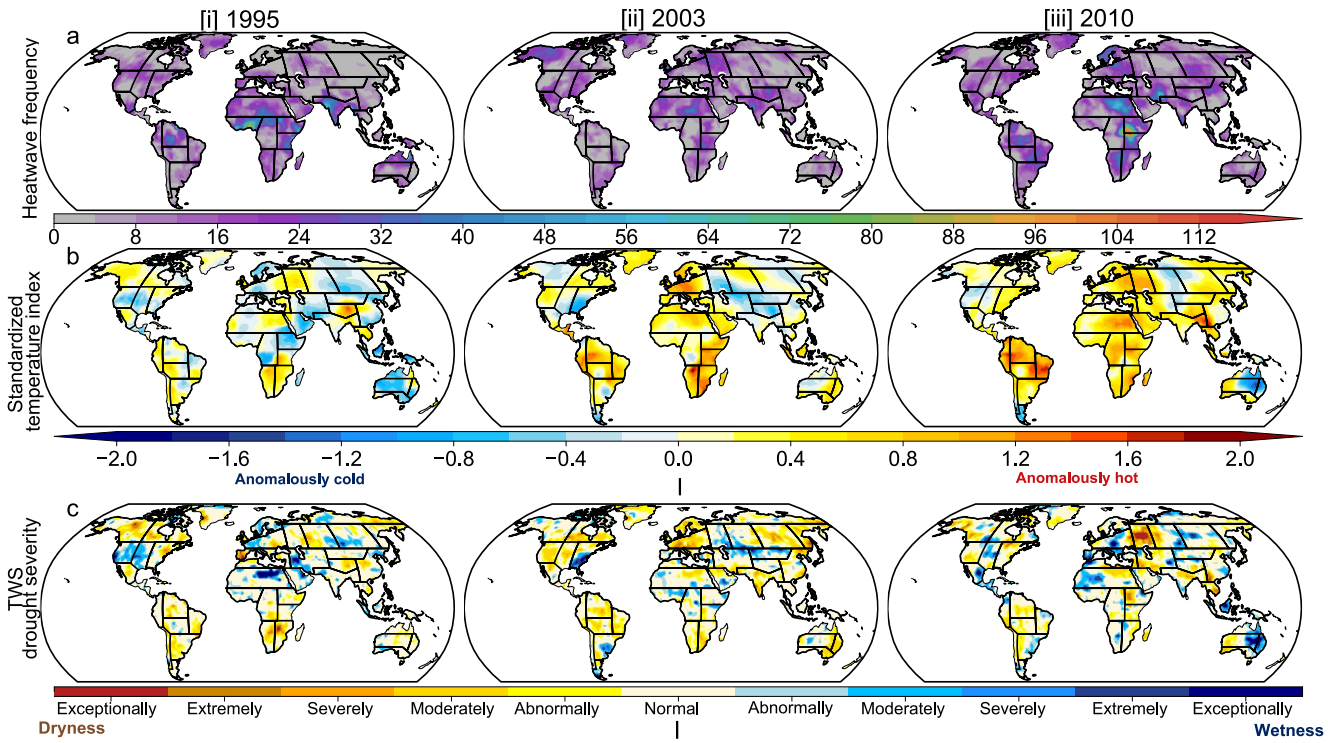

Figure 6. Spatial representation of key climatic and terrestrial indicators for (a) Heatwave Frequency, (b) Standardized Temperature Index (STI), and the cascading impact on, and (c) Terrestrial Water Storage-based Drought Severity Index (TWS-DSI) during four notable heatwave summers: [i] 1995, [ii] 2003, and [iii] 2010.

heatwaves highlights the complexities of heatwave impacts, even in areas with relatively homogeneous climatic and geographical characteristics. The 2014 heatwaves caused severe agricultural losses, food insecurity, and economic hardships in some areas of Southern Africa (IPCC, 2022; Nick et al., 2022), while others remained largely unaffected. Consequently, it becomes imperative to understand these sub-regional characteristics to facilitate proper planning and mitigation strategies.

In Figure 5, we present the 2014 anomalous fields relative to the historical reference period for Western South Africa (WSAF) and Eastern South Africa (ESAF) to highlight the influence of moisture flux divergence/convergence, humidity, and geopotential heights on HWF. Regions with positive anomalous geopotential heights (e.g., the black rectangle in Figure 5a) show reduced moisture flux convergence and negative anomalous RH, conditions that intensify HWF (Figure 5b). In contrast, areas with negative anomalous HWF (e.g., the red rectangle in Figure 5a) are characterized by strong low-level moisture convergence, negative anomalous geopotential height, and positive anomalous RH, collectively suppressing HWF.

This case study ties directly to the broader analysis mirroring WNA's reliance on dynamic processes (e.g., subsidence), and SAM's sensitivity to moisture transport. The EOT analysis (Figures 5c–5f) further shows that thermodynamic and dynamic drivers alternately dominate HWF peaks, akin to SAM and CAF regions. This analysis identifies a pivotal vertically integrated moisture flux convergence (VIMFC) signal (Figure 5ci) that accounts for 29% of the HWF variance (Figure 5ciii). The VIMFC signal is most prominent between 1993 and 1999, where HWF amplifies south of the signal and diminishes to the north (Figure 5cii). Additionally, this signal closely aligns with the maximum IVT (Figure 5ci), underscoring the critical link between moisture transport and HWF development. We extend the EOT to the thermodynamic and dynamic components of VIMFC (Figures 5di, 5dii, 5ei, 5eii) revealing that the thermodynamic term's signal of the EOT mode explains 25% of the HWF variance (Figure 5diii), emphasizing the importance of local energy exchanges and heating processes. However, the prominence of this signal varies over time, with positive and negative values reflecting stronger or weaker spatial patterns associated with the EOT mode. The dynamic term's EOT signal accounts for 30% of the variance (Figure 5eiii), highlighting the significant influence of atmospheric circulation patterns on HWF dynamics in the region. Notably, the dynamic term's strongest signal emerges in 1984. Peaks in HWF (Figure 5f) and EOT series

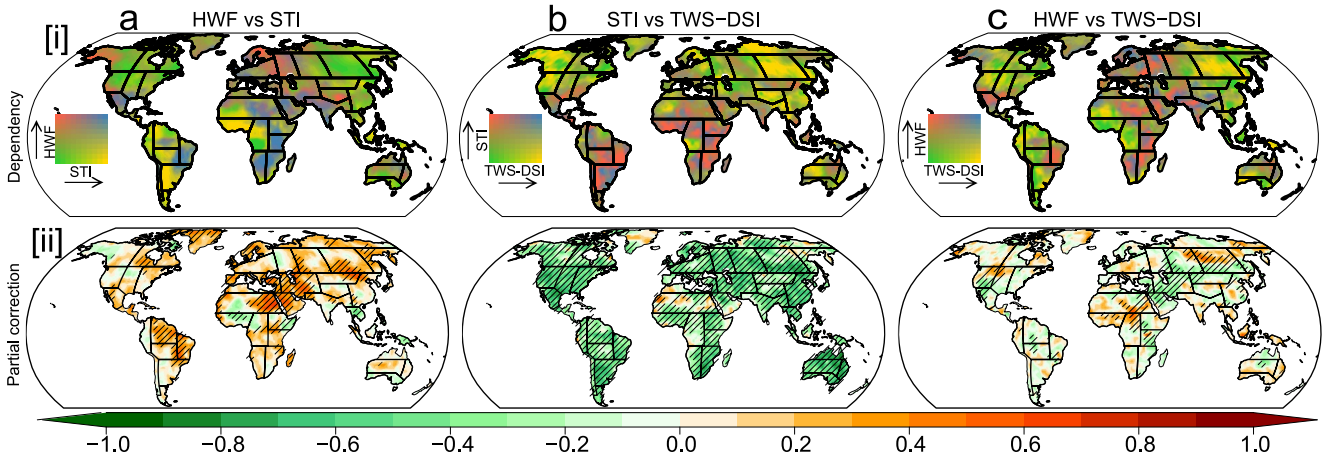

Figure 7. [i] Dependency between (a) Heatwave Frequency (HWF) and Standardized Temperature Index (STI), (b) STI and TWS-DSI during the historical period, and (c) HWF and Terrestrial Water Storage Drought Severity Index (TWS-DSI), [ii] partial correlation between these events. Striplings represent significant correlations at a 95% confidence level.

(Figures 5c–5eiii) during specific years highlight distinct contributions from the thermodynamic and dynamic terms. For instance, the dynamic term drives the HWF peak in 1980, while both thermodynamic and dynamic terms contribute to the peak in 2005. In contrast, the attenuated HWF magnitude observed in 1996 aligns with a reduction in that year's dynamic term. Similarly, the HWF peak in 1995 corresponds to positive thermodynamic and dynamic EOT patterns. These findings illustrate the complex dynamic and thermodynamic factors, each exerting unique influences on regional HWF dynamics and can be extrapolated to regions having similar dynamic and thermodynamic properties as ESAF and WSAF.

3.5. Synergistic Relationship Between Heatwaves, Temperature Anomaly, and Terrestrial Drought Severity

Figure 6 depicts the interrelationships between HWF, STI, and TWS-DSI during three notable heatwave years (1995, 2003, and 2010), emphasizing the cascading consequences of climate extremes. For example, our investigation of the 2003 Western Central European heatwave—one of the most intense on record (Figure 6a ii)—elevated STI across the region (Figure 6b ii), reinforcing the direct relationship between HWF and temperature anomalies. This persistent heatwave led to widespread soil moisture depletion and declining groundwater levels, reflected in severe TWS drought severity (Figure 6c iii). Similarly, in 2010, Eastern North America witnessed a combination of high HWF (Figure 6a i) and positive STI (Figure 6b ii), translating into TWS deficits (Figure 6c iii). However, Western North America in 1995 presents a contrasting case (Figure 6a i, 6b i, 6c i). High HWF coincides with anomalously cold STI and wet conditions, demonstrating that high HWF does not always imply widespread drying. This suggests that localized heatwaves can occur without significant TWS depletion. The wet TWS-DSI conditions support this, indicating that sufficient TWS likely moderated the hydrological impacts. The combination of cold STI and wet TWS-DSI may reflect a delayed seasonal transition, possibly due to delayed snowmelt in high-elevation areas (Figure A1c). This sustains wet TWS-DSI while suppressing broader temperature anomalies, resulting in localized heatwaves despite a regionally cold temperature. The cold regional STI may be explained by cold air advection from a downstream trough in the meandering jet stream (Figure A1b), creating a situation where high-pressure blocking induced localized heatwaves while cooler air masses dominated the broader region (Figures 2a and 2b). These factors demonstrate how regional atmospheric and hydrological processes can interact to produce seemingly contradictory signals in climatic indicators.

Furthermore, Figures 7a–7c presents a climatological analysis of the cascading impacts of HWF and STI on TWS drought severity index (TWS-DSI). Regions such as NES, WSAF, ARP, ESAF, and SEAF (Figure 7a) exhibit high HWF and STI, leading to increased TWS-DSI (Figure 7b), thus exacerbating drought conditions and creating a positive feedback loop where drought intensifies heatwaves by promoting conditions that accelerate soil moisture loss and reduce surface transpiration, ultimately amplifying air temperature (Figure 2j). In contrast, the WAF region displays high STI but lower HWF and TWS-DSI. Moreover, some regions (e.g., western WCE and

10.1029/2025EF006486

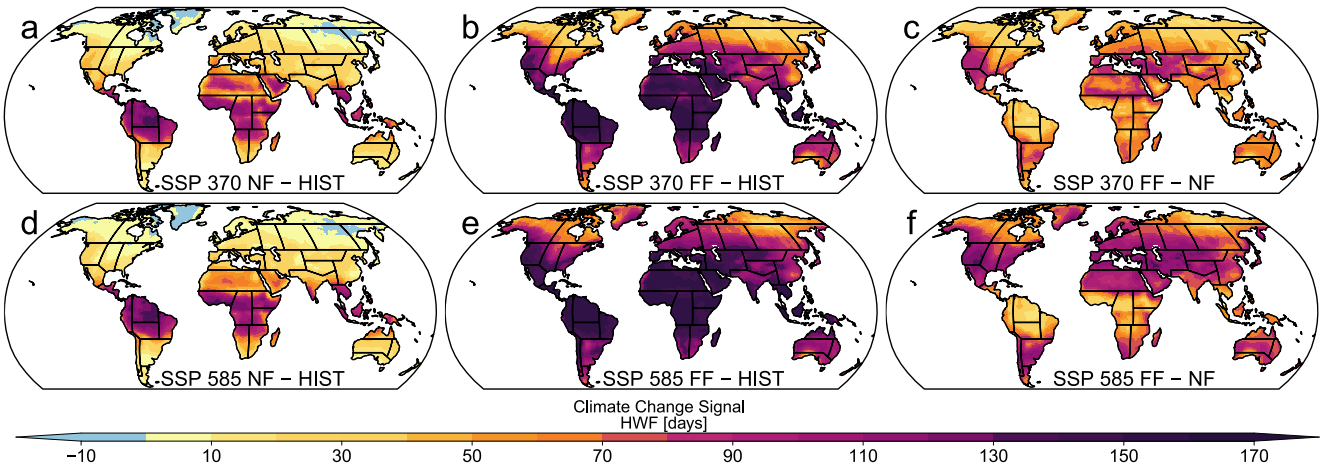

Figure 8. Climate change signal of heatwave frequency for (a) SSP 370 near future versus Historical period, (b) SSP 370 far future versus Historical period, (c) SSP 370 far future versus SSP 370 near future, (d) SSP 585 near-future versus Historical period, (e) SSP 585 far future versus Historical period, and (f) SSP 585 far future versus SSP 585 near future.

eastern NWN, as seen in Figures 2g and 7c) exhibit a clear positive correlation between HWF and TWS-DSI. This non-uniformity implies that factors beyond HWF—including atmospheric circulation patterns, soil moisture dynamics, and vegetation cover—play significant roles in modulating the overall impact of heatwaves on drought conditions. In areas where HWF appears to drive higher TWS-DSI, the inference is that heatwaves likely accelerate soil desiccation and suppress transpiration, thus amplifying warming conditions. Conversely, in regions where factors such as increased precipitation (Figure 2k) are more dominant, the detrimental effects of heatwaves on drought severity tend to be offset.

Overall, while the spatial associations between high HWF, elevated STI, and increased TWS-DSI are consistent with the presence of potentially self-reinforcing feedbacks between heatwaves and drought, it is important to emphasize that our evidence is inferential. Direct demonstration of these feedback mechanisms would require further process-based studies and dynamical modeling analyses. The current results, therefore, suggest potential pathways for such feedback rather than conclusively proving their occurrence.

3.6. Climate Change Signals in Heatwave

Understanding the climate change signals (CCS) of heatwaves is crucial for building resilience and adapting to a changing climate. Figures 8a–8f illustrates the CCS of HWF from historical to future periods. The analysis of HWF CCS from the historical period to the near future under SSP 370 (Figure 8a) shows an increase of over 100 days in most tropical regions relative to the historical period (e.g., NSA, NES, SAM, WAF, SAH, ARP). This increase becomes even more pronounced in the far future under SSP 370, with a rise of over 160 days (Figure 8b). The most notable changes from the near to far future occur in WNA, NCA, WCA, MED, and SAH (Figure 8c). Moreover, the CCS analysis from the historical period to the far future under SSP 585 (Figure 8e) reveals the most striking signals, with many regions experiencing unprecedented increases in HWF, exceeding 170 days in SAH, NSA, WAF, CAF, SCA, and SEA. Furthermore, the transition from the near future to the far future under SSP 585 (Figure 8f) shows that, except for NSA, NES, SAM, WAF, and CAF, all regions will experience positive signals, with increases of over 30 HWF days.

3.7. Population Exposure to Heatwaves

Figures 9a–9g illustrates the varying total population exposure to HWF during historical and future periods. During the historical period (Figure 9a), most African regions exhibit exposure levels ranging from 100 to 500 person-days, contributing to a cumulative total of approximately 20 million person-days across the continent (Figure 9g). In contrast, the Asian continent witnesses a broader spectrum of exposure levels, spanning from 100 to over 5,000 person-days (Figure 9a), resulting in a total of 50 million person-days of exposure (Figure 9g). Regionally, South Asia and Eastern Central Asia stand out with exposure exceeding 5,000 person-days (Figure 9a), culminating in 25 million person-days (Figure 9f). Moreover, future projections indicate a notable

10.1029/2025EF006486

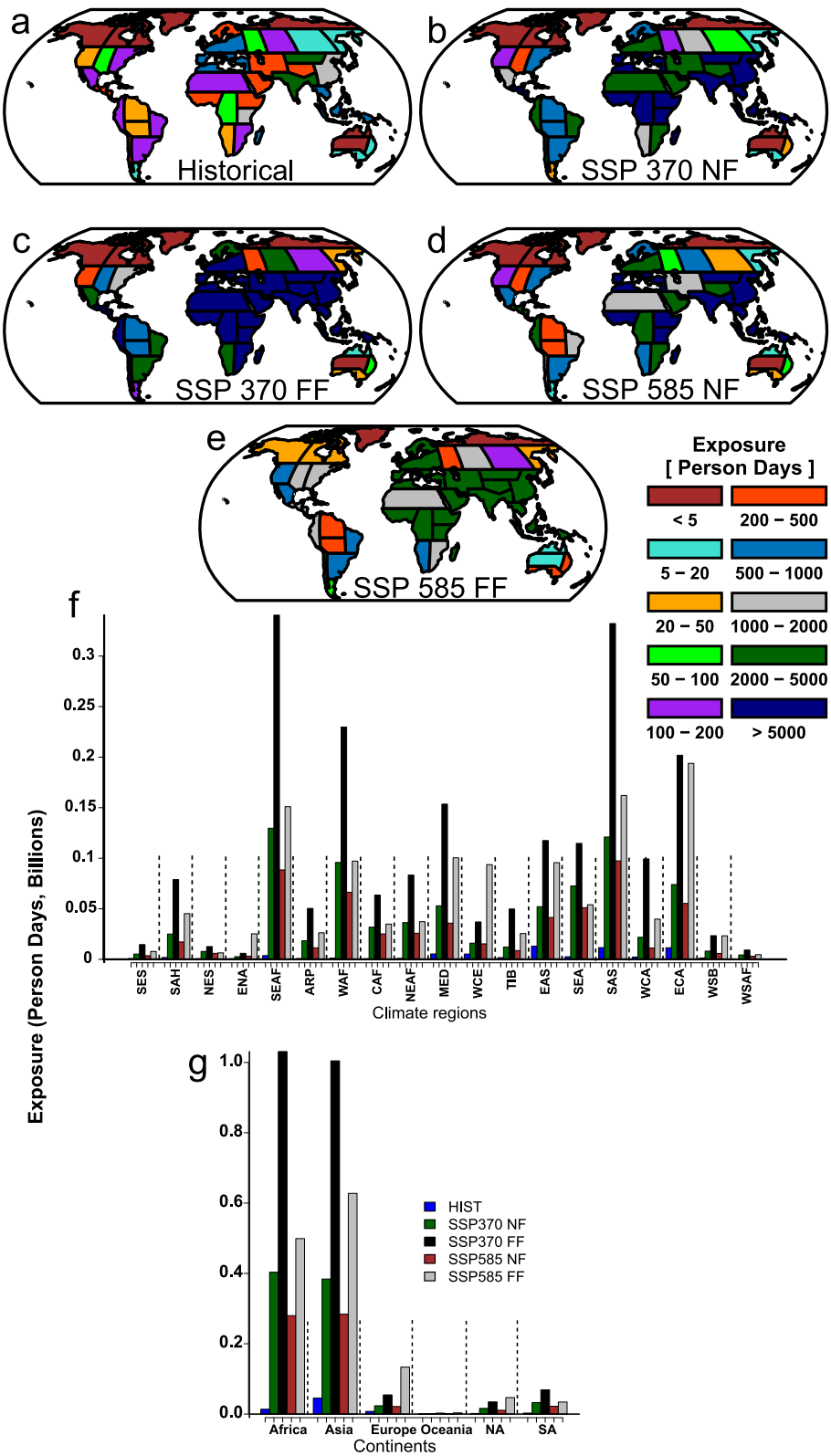

Figure 9. Total population exposure to heatwave frequency during (a) historical period, (b) near future under SSP 370, (c) far future under SSP 370, (d) near future under SSP 585, (e) far future under SSP 585, (f) climate regions, and (g) continental-scale during historical and future periods.

10.1029/2025EF006486

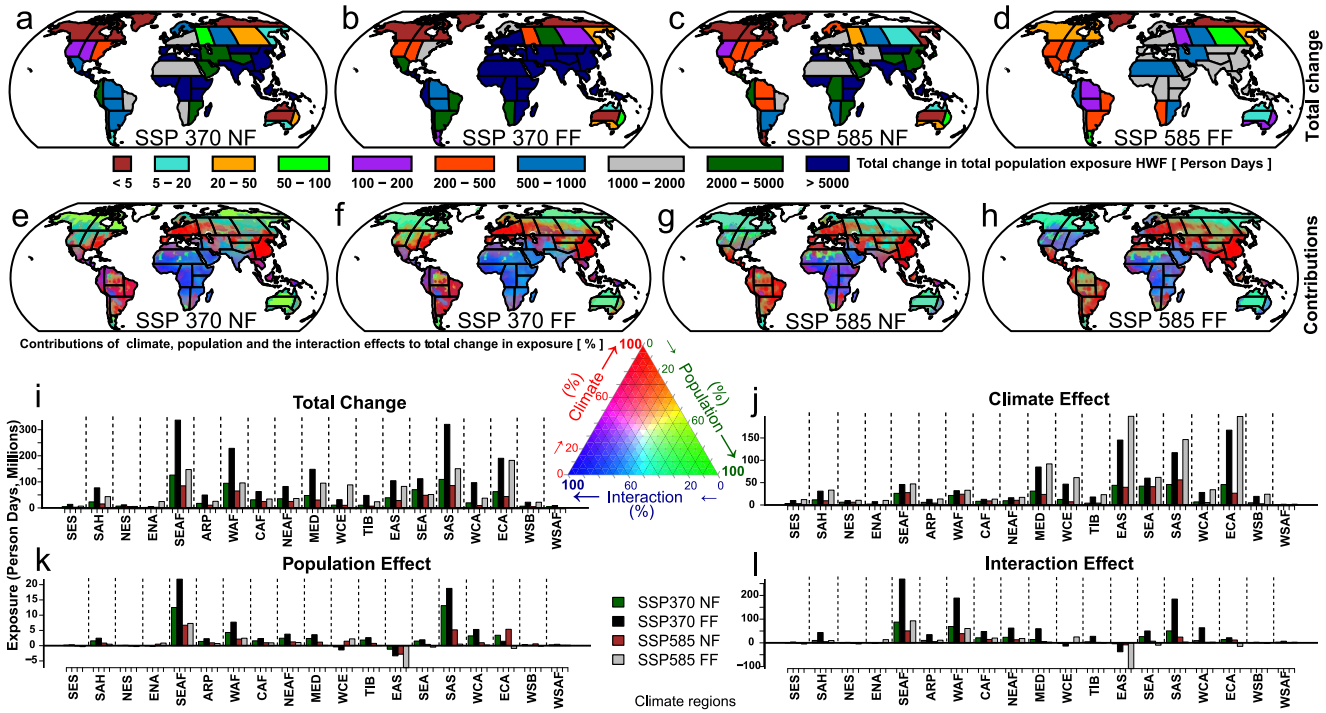

Figure 10. The total change in total population exposure to heatwave frequency as a result of climate, population, and interaction effects during (a) near-future under SSP 370, (b) far future under SSP 370, (c) near future under SSP 585, (d) far future under SSP 585, (e, f, g, h) Contributions of climate, population, and interaction effects to the total change in population exposure, and (i, j, k, l) Climate region heatwave exposure due to total change, climate effect, population effect, and interaction effect, respectively.

escalation in exposure levels across various regions. For example, Southern East Africa, West Africa, Eastern Asia, Southern Asia, and Eastern Central Asia will witness more than 100% rise in the exposure level in the future under SSP 370 and 585 (Figure 9f). A comparative analysis between the historical (Figure 9a) and the SSP 370 future scenario (Figures 9b–9g) reveals a considerable increase in exposure, particularly in tropical regions of Africa and Asia. Notably, the far future projection under SSP 370 (Figure 9c) portrays a more widespread distribution of high exposure than the near future projection (Figure 9b), culminating in 400 million and over one billion person-days in Africa during the near and far future, respectively (Figure 9g). Similarly, a parallel observation is made in the SSP 585 future scenarios (Figures 9d and 9e), totaling over 600 million person-days in Asia under SSP 585 far future (Figure 9g). However, it is worth highlighting that the SSP 370 far future scenario generally anticipates the most extensive high heatwave exposure across the analyzed regions (Figures 9f and 9g).

Furthermore, we observe regional disparities in the projected total change of population exposure to heatwaves from historical to future periods (Figures 10a–10l). For example, under SSP 370, Eastern Central Asia exhibits a total change in population exposure to heatwaves between 2000 and 5,000 person-days (Figure 10a), amounting to 60 million person-days (Figure 10i) as a result of climate, population, and the interaction between the two effects during the near future. This is unlike the far future (Figure 10b), which projects over 5,000 person-days, totaling 195 million person-days (Figure 10i). The contributions of climate, population, and their interaction reveal distinct regional patterns in projected changes to total heatwave exposure (Figures 10e–10h). In West Africa, for example, the near future under SSP 370 exhibits an evident domineering interaction effect (at 80%), accounting for over 60 million person-days (Figures 10e and 10l). In comparison, climate contributes 10% and population 10%, amounting to 16 million and 5 million person-days, respectively (Figures 10j and 10k). In all scenarios, climate effect contributes more than 80% in East Asia (Figures 10e–10h), amounting to 48 million, 149 million, 46 million, and 180 million person-days under SSP 370 near and far-future, and SSP 585 near and far-future, respectively (Figure 10j). East and Eastern Central Asia will generally experience the most total change due to climate effects (Figures 10i and 10j). Southern East Africa and Southern Asia will witness the highest total change due to population effects (Figures 10i and 10k). Notably, East Asia will witness negative population contributions to the total change in population exposure to heatwaves in the future (Figure 10k).

4. Discussion

This study highlights the need to consider regional specificities in assessing heatwave dynamics and impacts. While global climate models provide valuable insights into heatwave projections, their limitations, such as coarse resolution and oversimplified representations of key processes, restrict them from impact studies. Although BC methods like MBCN can enhance model accuracy (Adeyeri, Zhou, Ndehedehe, Wang, & Ishola, et al., 2024; Dieng et al., 2022), its iterative nature makes it computationally expensive (Adeyeri et al., 2020).

Nevertheless, the unique atmospheric and environmental interactions that drive heatwaves require targeted regional analyses. The distinct interplay of factors influencing heatwaves varies significantly across regions, making generalizations potentially misleading. Regions like NEU, and ECA with positive MFD influence are consistent with HWF-RH negative relationship at near-surface, signaling conducive conditions for dry heatwave conditions, as drier conditions at the surface raise air temperature through land-atmosphere feedback (e.g., Seneviratne et al., 2010). The negative MFD correlation, which may suggest net moisture gain at the surface, is consistent with the wind patterns with moisture-laden air transport toward regions like the NSA, SSA, WCE, and ARP. However, this does not translate into more evaporation and suppression of heatwaves in these regions. The HWF-RH positive relationships suggest that the increased moisture or water vapor content is likely trapping heat at the surface, enhancing air temperature and heatwave conditions. These interactions coincide with humid heatwave conditions common in tropical and subtropical regions where moist heat plays a role (Ha et al., 2022; Raymond et al., 2020).

Significant positive correlations between VIMFD and HWF correspond to regions with significant positive thermodynamic responses (e.g., SAM, ECA, and East Africa), aligning with existing research demonstrating the influence of thermodynamic effects, particularly RH, on temperature extremes (Krueger et al., 2015), and future heatwave projections (Vogel et al., 2020). In contrast, WCA exhibits moisture divergence driven by significant positive dynamic effects, which correlates with increased HWF. This is physically consistent, as drier conditions resulting from dynamic moisture divergence limit evaporative cooling, allowing for more efficient heating of the surface and near-surface atmosphere, thus fueling heatwaves (Ha et al., 2022). Furthermore, in West Africa and the Sahara, the heatwave dynamics are shaped by a compound interaction of atmospheric processes, including the lower tropospheric southwestern moisture flow from the Atlantic ocean, the tropospheric monsoon trough, a weak ridge spanning the Mediterranean, the mid-tropospheric Saharan high to the west (Adeyeri, Zhou, Ndehedehe, Wang, & Ishola, et al., 2024), and the intensified southward moisture transfer by the AEJ (Cook, 1999). Low tropospheric cut-off lows (Konapala et al., 2020), low-level Jet (Trenberth et al., 2009), and tropical cyclones regulate heatwaves through moisture fluxes in the Madagascar region. In general, atmospheric rivers and monsoonal moisture flux facilitate the transport of excess moisture into different regions (Aalgarra et al., 2020; Adeyeri, Zhou, Ndehedehe, Wang, & Ishola, et al., 2024), impacting TWS and thus modulating heatwaves.

Terrestrial water storage encompasses groundwater, soil moisture, and surface water, significantly influencing climate, particularly heatwave dynamics. Groundwater is pivotal to land surface conditions (Ndehedehe, Adeyeri, et al., 2023), especially during heatwaves, influencing soil moisture and evaporative cooling. Adequate soil moisture mitigates heatwave severity (Adeyeri, Zhou, Ndehedehe, & Wang, 2024), while groundwater discharge can directly cool the land surface (Chen & Hu, 2004), particularly in regions with abundant groundwater (Ndehedehe, Adeyeri, et al., 2023, Ndehedehe, Ferreira, et al., 2023). Furthermore, groundwater-released moisture can influence the atmospheric boundary layer, affecting atmospheric stability and heatwave development (Mu et al., 2021). Similarly, the relationship between HWF and TWS-DSI is complex, as higher HWF does not always amplify drought, whereas positive STI often does. This complexity arises from delayed seasonal transitions, altered atmospheric circulation, and human activities, which create localized feedback loops that exacerbate climatic stress. For instance, during the 1995 heatwave in Western North America, atmospheric blocking, high humidity, subsidence, and wet hydrological conditions from delayed snowmelt or preceding winter precipitation (Kunkel et al., 1996; NOAA, 2020) sustained TWS, leading to elevated HWF, anomalously cold STI, and wet conditions. Moreover, water stored within the terrestrial system may not be readily accessible or efficiently distributed to mitigate heatwave impacts, and the timing and intensity of heatwave events may exceed the buffering capacity of existing TWS (Wang et al., 2019). These interactions highlight how regional atmospheric and hydrological processes can produce contradictory climatic signals.

Additionally, regions with positive anomalous geopotential height exhibit lower-level moisture flux convergence and negative anomalous RH, translating to positive anomalous HWF. This often indicates a high-pressure system,

causing air to sink and warm up as it descends. This tends to reduce cloud formation and RH (Ad & Zuo, 2021; Fischer et al., 2021), resulting in hot and dry conditions that increase the likelihood and intensity of heatwaves. Overall, negative anomalous geopotential height is often associated with reduced heatwaves.

Despite projecting, at least, a fourfold increase in future HWF, exposure to heatwave depends on various factors beyond just temperature. Changes in synoptic circulation patterns (Ad & Zuo, 2021), meteorological conditions (Luo et al., 2022), local topography, demographics, and land use changes (Adeyeri, Folorunsho, et al., 2024; Findell et al., 2017) all play critical roles, but population dynamics are particularly crucial. Generally, SSP 370 far future scenario projects the most widespread high heatwaves exposure due to a significant population boom in the second half of the century under SSP 370 (Jones & O'Neill, 2016; Riahi et al., 2017). Moreover, Southern East Africa, South Asia, Eastern Central Asia, and West Africa are expected to experience over 100% change in total population exposure compared to other regions, especially under SSP 370 far future. Furthermore, the interaction between climate and population effects contributes to the total change in population exposure to heatwaves, which is generally higher in most African regions under all scenarios. For most regions in Southern America and Europe, the climate effect dominates, highlighting the critical need for practical climate actions to address the human population's exposure to heatwaves. South Eastern Africa stands to experience the highest total change in heatwave exposure due to combined climate, population, and interaction effects under the SSP 370 far future scenario. Moreover, we observe the maximum climate effects in East Asia under the SSP 585 far future scenario. This underscores the need for a holistic approach to evaluating population vulnerability to heatwaves. Vulnerability is a function of society's exposure, sensitivity, and hazard adaptability (Jones et al., 2015). These three aspects will undoubtedly change over time, potentially influencing the risk from heatwaves.

Our analysis did not distinguish urban and rural temperature change due to urbanization, which can differ substantially due to urban heat island effect (Adeyeri, Zhou, et al., 2022; Shao et al., 2023). However, our findings hold critical implications for decision-makers across different sectors. For example, we associate wetter conditions with more frequent heatwaves in some areas, as evidenced by a positive correlation between the TWS-DSI and HWF. As a result, heatwaves may facilitate more evapotranspiration, enhancing cloud formation and precipitation conditions (Miralles et al., 2019). On the other hand, areas with negative correlations indicate higher soil moisture impact on heatwave through energy partitioning. As heatwaves intensify, drying soil restricts plant transpiration (Wang et al., 2019), favoring sensible heat transfer (direct air warming) over latent heat release (evaporation). This further diminishes soil moisture, inhibits cloud formation, and aggravates heatwaves (Wang et al., 2019). Our observation of reduced TWS coinciding with heightened HWF in most regions corroborates this phenomenon. These dynamics underscore the potential for heatwaves to exacerbate droughts and deplete water resources (Ndehedehe & Adeyeri, 2024). Consequently, ecosystems face heightened strain, leading to biodiversity loss and even local extinctions (In Pachauri & Mayer, 2015).

5. Conclusion

This study enhances understanding of heatwave dynamics in a warming world by integrating large-scale atmospheric processes, and regional variability. By identifying dominant drivers—such as thermodynamic instability in monsoonal regions, TWS impacts in semi-arid zones, and dynamic subsidence in subtropical ridges—it moves beyond generic resilience strategies to enable regionally tailored solutions. These insights are critical as climate change intensifies heatwave risks, which are further compounded by the synergistic relationship between demographic and socioeconomic factors.

We emphasize that adaptation measures must directly address the dominant regional mechanisms driving heatwaves. For example, WAF region should prioritize soil moisture retention through agroforestry and groundwater management to counteract TWSs contribution to HWF. SAM region should strengthen early warning systems for monsoon breaks and enforce land-use policies that preserve vegetation to mitigate thermodynamic instability. To address dynamic ridge amplification, WNA region should integrate urban cooling infrastructure (e.g., reflective surfaces and green corridors) with synoptic-scale monitoring. In addition, urban planning must balance population growth with climate resilience in hotspot regions like Southern Africa, South Asia, and East Asia. This includes decentralizing high-density settlements, expanding cooling centers, and improving healthcare access. Meanwhile, transboundary cooperation in East Asia is essential to regulate pollutants (e.g., aerosols, methane) that disrupt atmospheric moisture balance and exacerbate heatwaves. Under high-emission scenarios (e.g., SSP585), preemptive infrastructure investments in regions like the Sahara and Central Africa should leverage

driver-specific diagnostics to optimize preparedness. Finally, sustained community involvement is vital to ensure solutions are culturally relevant and equitably implemented. Participatory approaches, such as co-designing heat action plans with local stakeholders, can bridge gaps between technical projections and lived experiences, fostering trust and long-term resilience.

Appendix A: Multivariate Bias-Correction Employing an N-Dimensional Probability Density Function Transform

The multivariate bias correction (BC) method uses the quantile mapping technique to adjust the marginal distributions of climate model simulations while maintaining the expected changes in simulated quantiles (Adeyeri et al., 2020; Cannon, 2018). The multivariate rescaling approach uses N-dimensional probability density function transform (MBCN) to modify the joint multivariate dependence structure between dependent variables in multivariate BC following the QDM approach (Adeyeri et al., 2020, Adeyeri, Zhou, Ndehedehe, Wang, & Ishola, et al., 2024).

The MBCN utilizes QDM to enhance the N-dimensional probability density function transform approach by incorporating data from $R_{m,c}, R_{m,p}$ and $R_{o,c}$. The $R_{m,c}, R_{m,p}$ and $R_{o,c}$ variables are rotated, and the absolute change from Equations A5 and A6 are applied to each rotated $R_{m,c}, R_{m,p}$ and $R_{o,c}$ variables. Consequently, the spun $R_{m,c}, R_{m,p}$ and $R_{o,c}$ are rotated back as $R_{m,c}^{[t+1]}, R_{m,p}^{[t+1]}, R_{o,c}^{[t+1]}$. This operation repeats itself until $R_{m,c}^{[t+1]}$ equals $R_{o,c}$. Each column of $R_{m,p}$ is ranked following the ordinal rankings of the corresponding elements in each column of $R_{m,p}^{[t+1]}$ to maintain trends in $R_{m,p}$ (Adeyeri, Zhou, Ndehedehe, Wang, & Ishola, et al., 2024):

The relative change in quantiles between the calibration and projected periods (t) for conservative variables:

$$\Delta(t_c) = \frac{F_{m,p}^{[t-1]}[\varepsilon(t)]}{F_{m,c}^{-1}[\varepsilon(t)]} \tag{A1}$$

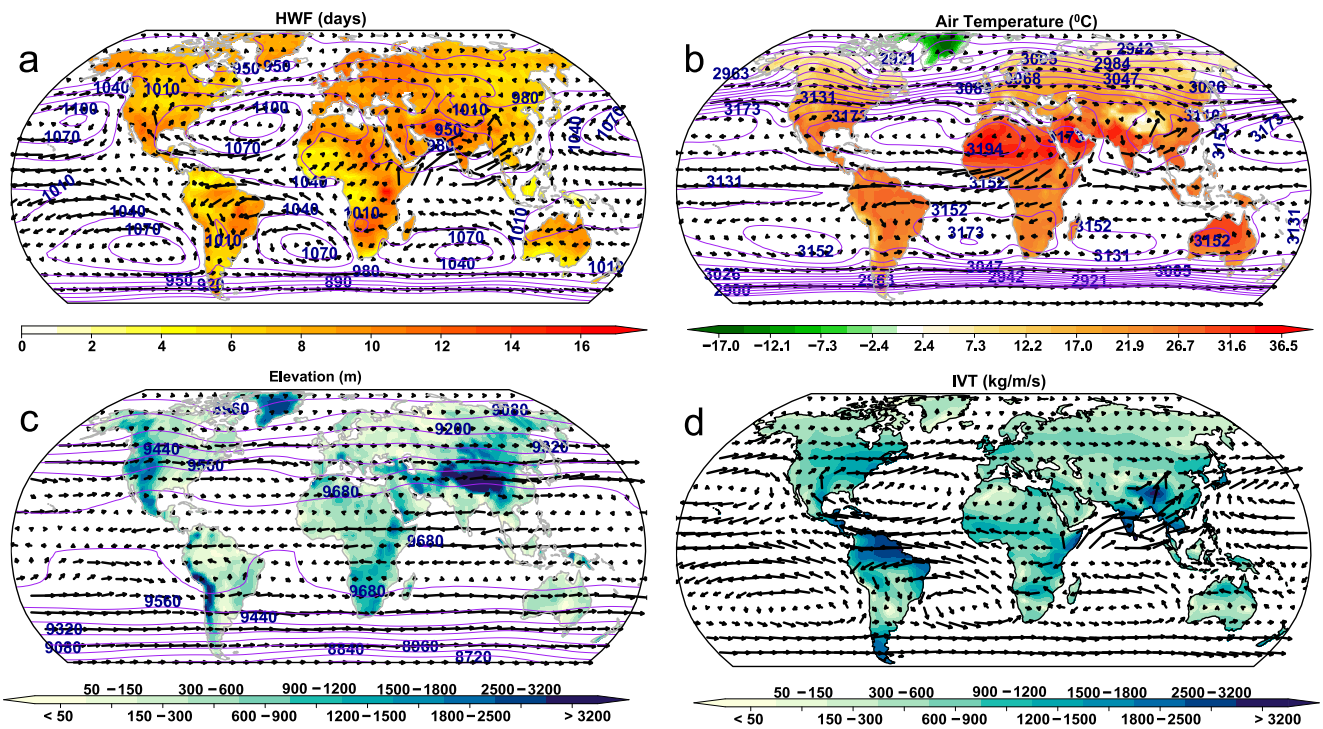

Figure A1. Long-term average state from 1979 to 2014 of (a) heatwave frequency, Vapor transport (VT) (vectors), and geopotential heights (contours) at 925 hPa, (b) Air temperature, VT (vectors), and geopotential heights (contours) at 700 hPa, (c) Elevation, VT (vectors), and geopotential heights (contours) at 300 hPa, and (d) Vertically integrated moisture transport (Integrated vapor transport) from 300 to 1,000 hPa.

The relative change in quantiles between the calibration and projected periods (t) for non-conservative variables:

$$\Delta(t_{nc}) = F_{m,p}^{[t-1]}[\varepsilon(t)] - F_{m,c}^{-1}[\varepsilon(t)] \tag{A2}$$

The non-exceedance probability (ε) associated with variable x at time t is given as:

$$\varepsilon(t) = F_{m,p}^{(t)}[x_{m,p}(t)] \tag{A3}$$

$x_{m,p}(t)$ is the climate model value m within the projection period p, $F_{m,p}^{(t)}$ is the time-dependent cumulative distribution function (CDF) of the climate model projection $x_{m,p}$. Using a 30 year moving window, $x_{m,p}$ was calculated based on the empirical CDF. $F_{m,c}^{[t-1]}$ is the simulations' inverse CDF during the calibration periods.

The model's ε quantile is bias-corrected from observation across the calibration period:

$$\hat{x}(t) = F_{o,c}^{[t-1]}[\varepsilon(t)] \tag{A4}$$

where $\hat{x}$ is the bias-corrected quantile.

The inverse CDF during the calibration period, $F_{o,c}^{[t-1]}$ was calculated from observation $x_{o,c}$.

The final bias-corrected model projection x_c at a time t is given as (Adeyeri, Zhou, Ndehedehe, Wang, & Ishola, et al., 2024).

$$x_c(t) = \hat{x}(t)\,\Delta\,(t), \text{for conservative variable} \tag{A5}$$

$$x_c(t) = \hat{x}(t) + \Delta(t), \text{for non-conservative variable} \tag{A6}$$

Appendix B: The Relative Contribution of Environmental Variables to Heatwave Frequency

The HWF and environmental variables are subjected to CPI and presented as (Adeyeri, Laux, et al., 2022; Strobl et al., 2008).

1. For the regression trees in the random forest

$$R^{(t)} = \sum_{i\in\beta^{(t)}} \frac{\left(\hat{y}_i^{(t)} - y_i\right)^2}{\left|\beta^{(t)}\right|} \tag{B1}$$

$$R_{(k)}^{(t)} = \sum_{i\in\beta^{(t)}} \frac{\left(\hat{y}_{i(k)}^{(t)} - y_i\right)^2}{\left|\beta^{(t)}\right|} \tag{B2}$$

2. For the classification trees in the random forest

$$R^{(t)} = \sum_{i\in\beta^{(t)}} \frac{I\left(\hat{y}_i^{(t)} \neq y_i\right)}{\left|\beta^{(t)}\right|} \tag{B3}$$

$$R_{(k)}^{(t)} = \sum_{i\in\beta^{(t)}} \frac{I\left(\hat{y}_{i(k)}^{(t)} \neq y_i\right)}{\left|\beta^{(t)}\right|} \tag{B4}$$

$$\hat{y}_{i(k)}^{(t)} = f^{(t)}(x_{i(k)}) \tag{B5}$$

$$x_{i(k)} = (x_i 1, \ldots, x_{ik-1}, x_{p(i)k}, x_{ik+1}, \ldots, x_{ip})$$

where $R^{(t)}$ and $R_{(k)}^{(t)}$ are the prediction error of tree t in a random forest with predictors p and ntrees of trees based on the out-of-bag sample $\beta^{(t)}$, respectively, before the permutation of the out-of-bag values of X_k. $\left|\beta^{(t)}\right|$ is the out-of-bag cardinal number sample for tree t, and $I()$ is the indicator function.

$\hat{y}_i^{(t)}$ is the function $f^{(t)}(x_i)$, which is the random forest prediction of the out-of-bag observation i before permutation. $x_{p(i)k}$ is the ith X_k observation after permutation.

The forest permutation of importance $PI_{(k)}$ is the average overall tree-wise permutation $PI_{(k)}^{(t)}$.

$$PI_{(k)} = \frac{\sum_{t=1}^{ntree} PI_{(k)}^{(t)}}{ntree} \tag{B6}$$

where $PI_{(k)}^{(t)} = R_{(k)}^{(t)} = R^{(t)}$

In the CPI, out-of-bag values of one predictor $X_{(k)}$ are conditionally permuted on other predictors $Z_{(-k)}$.

Data Availability Statement

The CMIP6 data can be downloaded from the Earth System Grid Federation (ESGF) nodes via https://aims2.llnl.gov/search/cmip6.

The GFZ Data Services distribute the W5E5 reference dataset, and can be downloaded at Lange (2019).

The reconstructed GRACE data is publicly available at Humphrey and Gudmundsson (2019).

The JRA55 reference data is publicly available at Japan Meteorological Agency/Japan (2013).

The population data is publicly available at Jones and O'Neill (2016) and Franziska and Geiger (2017).

Software: All analyses and figures were drawn in the *R* Foundation for Statistical Computing version 4.2.2 Platform (R Core Team, 2022) and Python version 3.9 (Python Software Foundation).

Acknowledgments
This work is supported by the National Natural Science Foundation of China Grants (42288101, 42120104001). Christopher E. Ndehedehe is supported by the Australian Research Council Grant DE230101327. Oluwafemi E. Adeyeri is supported by the Australian Research Council Grant CE230100012. We thank the World Climate Research Programme for coordinating and promoting CMIP6 through its Working Group on Coupled Modelling.

References

Aalgarra, I., Nieto, R., Ramos, A. M., Eiras-Barca, J., Trigo, R. M., & Gimeno, L. (2020). Significant increase of global anomalous moisture uptake feeding landfalling Atmospheric Rivers. *Nature Communications*, *11*(1), 5082. https://doi.org/10.1038/s41467-020-18876-w

Acppelhans, T., Detsch, F., & Nauss, T. (2015). Remote empirical orthogonal teleconnections in R. *Journal of Statistical Software*, *65*(10). https://doi.org/10.18637/jss.v065.i10

Ad, N., & Zuo, Z. (2021). Investigating the influence of synoptic circulation patterns on regional dry and moist heat waves in North China. *Climate Dynamics*, *57*(3–4), 1227–1240. https://doi.org/10.1007/s00382-021-05769-x

Adeliyi, T. E., Akinsanola, A. A., Taguela, T. N., Adeyeri, O. E., & Singhai, P. (2025). Exploring Afro-Asian water fluxes in CMIP5 and CMIP6 models: Present-day evaluation and future projections. *Science of the Total Environment*, *977*, 179374. https://doi.org/10.1016/j.scitotenv.2025.179374

Adeyeri, O. E., Folorunsho, A. H., Ayegbusi, K. I., Bobde, V., Adeliyi, T. E., Ndehedehe, C. E., & Akinsanola, A. A. (2024a). Land surface dynamics and meteorological forcings modulate land surface temperature characteristics. *Sustainable Cities and Society*, *101*, 105072. https://doi.org/10.1016/j.scs.2023.105072

Adeyeri, O. E., Laux, P., Ishola, K. A., Zhou, W., Balogun, I. A., Adeyewa, Z. D., & Kunstmann, H. (2022). Homogenising meteorological variables: Impact on trends and associated climate indices. *Journal of Hydrology*, *607*, 127585. https://doi.org/10.1016/j.jhydrol.2022.127585

Adeyeri, O. E., Laux, P., Lawin, A. E., & Oyekan, K. S. A. (2020). Multiple bias-correction of dynamically downscaled CMIP5 climate models temperature projection: A case study of the transboundary Komadugu-Yobe river basin, lake Chad region, West Africa. *SN Applied Sciences*, *2*(7), 1221. https://doi.org/10.1007/s42452-020-3009-4

Adeyeri, O. E., Zhou, W., Laux, P., Ndehedehe, C. E., Wang, X., Usman, M., & Akinsanola, A. A. (2023). Multivariate drought monitoring, propagation, and projection using bias-corrected general circulation models. *Earth's Future*, *11*(4). https://doi.org/10.1029/2022EF003303

Adeyeri, O. E., Zhou, W., Laux, P., Wang, X., Dieng, D., Widana, L. A., & Usman, M. (2023). Land use and land cover dynamics: Implications for thermal stress and energy demands. *Renewable and Sustainable Energy Reviews*, *179*, 113274. https://doi.org/10.1016/j.rser.2023.113274

Adeyeri, O. E., Zhou, W., Ndehedehe, C. E., & Wang, X. (2024b). Global vegetation, moisture, thermal and climate interactions intensify compound extreme events. *Science of the Total Environment*, *912*, 169261. https://doi.org/10.1016/j.scitotenv.2023.169261

Adeyeri, O. E., Zhou, W., Ndehedehe, C. E., Wang, X., Ishola, K. A., & Laux, P. (2024c). Minimizing uncertainties in climate projections and water budget reveals the vulnerability of freshwater to climate change. *One Earth*, *7*(1), 72–87. https://doi.org/10.1016/j.oneear.2023.12.013

Adeyeri, O. E., Zhou, W., Wang, X., Zhang, R., Laux, P., Ishola, K. A., & Usman, M. (2022). The trend and spatial spread of multisectoral climate extremes in CMIP6 models. *Scientific Reports*, *12*(1), 21000. https://doi.org/10.1038/s41598-022-25265-4

Akinsanola, A. A., Adebiyi, A. A., Bobde, V., Adeyeri, O. E., Tamoffo, A. T., & Danso, D. K. (2025). Projected changes in African easterly wave activity due to climate change. *Communications Earth & Environment*, *6*(1), 2. https://doi.org/10.1038/s43247-024-01981-9

Barriopedro, D., Fischer, E. M., Luterbacher, J., Trigo, R. M., & García-Herrera, R. (2011). The hot summer of 2010: Redrawing the temperature record map of Europe. *Science*, *332*(6026), 220–224. https://doi.org/10.1126/science.1201224

Brás, T. A., Seixas, J., Carvalhais, N., & Jägermeyr, J. (2021). Severity of drought and heatwave crop losses tripled over the last five decades in Europe. *Environmental Research Letters*, *16*(6), 65012. https://doi.org/10.1088/1748-9326/abf004

Breiman, L. (2001). Random forests. *Machine Learning*, *45*(1), 5–32. https://doi.org/10.1023/A:1010933404324

Cannon, A. J. (2018). Multivariate quantile mapping bias correction: An N-dimensional probability density function transform for climate model simulations of multiple variables. *Climate Dynamics*, *50*(1–2), 31–49. https://doi.org/10.1007/s00382-017-3580-6

Cannon, A. J., Sobie, S. R., & Murdock, T. Q. (2015). Bias correction of GCM precipitation by quantile mapping: How well do methods preserve changes in quantiles and extremes? *Journal of Climate*, *28*(17), 6938–6959. https://doi.org/10.1175/JCLI-D-14-00754.1

Chen, X., & Hu, Q. (2004). Groundwater influences on soil moisture and surface evaporation. *Journal of Hydrology*, *297*(1–4), 285–300. https://doi.org/10.1016/j.jhydrol.2004.04.019

Clarke, B., Otto, F., Stuart-Smith, R., & Harrington, L. (2022). Extreme weather impacts of climate change: An attribution perspective. *Environmental Research: Climate*, *1*(1), 12001. https://doi.org/10.1088/2752-5295/ac6e7d

Cook, K. H. (1999). Generation of the African easterly jet and its role in determining west African precipitation. *Journal of Climate*, *12*(5), 1165–1184. https://doi.org/10.1175/1520-0442(1999)012%3C1165:GOTAEJ%3E2.0.CO;2

Cucchi, M., Weedon, G. P., Amici, A., Bellouin, N., Lange, S., Müller Schmied, H., et al. (2020). WFDE5: Bias-adjusted ERA5 reanalysis data for impact studies. *Earth System Science Data*, *12*(3), 2097–2120. https://doi.org/10.5194/ESSD-12-2097-2020

Déqué, M., Rowell, D. P., Lüthi, D., Giorgi, F., Christensen, J. H., Rockel, B., et al. (2007). An intercomparison of regional climate simulations for Europe: Assessing uncertainties in model projections. *Climatic Change*, *81*(S1), 53–70. https://doi.org/10.1007/s10584-006-9228-x

Dieng, D., Cannon, A. J., Laux, P., Hald, C., Adeyeri, O., Rahimi, J., et al. (2022). Multivariate bias-correction of high-resolution regional climate change simulations for West Africa: Performance and climate change implications. *Journal of Geophysical Research: Atmospheres*, *127*(5). https://doi.org/10.1029/2021JD034836

Findell, K. L., Berg, A., Gentine, P., Krasting, J. P., Lintner, B. R., Malyshev, S., et al. (2017). The impact of anthropogenic land use and land cover change on regional climate extremes. *Nature Communications*, *8*(1), 989. https://doi.org/10.1038/s41467-017-01038-w

Fischer, E. M., Sippel, S., & Knutti, R. (2021). Increasing probability of record-shattering climate extremes. *Nature Climate Change*, *11*(8), 689–695. https://doi.org/10.1038/s41558-021-01092-9

Franziska, P., & Geiger, T. (2017). ISIMIP2a population input data (v1.0). *ISIMIP Repository*. https://doi.org/10.48364/ISIMIP.523208

Ha, K.-J., Seo, Y.-W., Yeo, J.-H., Timmermann, A., Chung, E.-S., Franzke, C. L. E., et al. (2022). Dynamics and characteristics of dry and moist heatwaves over East Asia. *NPJ Climate Atmosphere Science*, *5*(1), 49. https://doi.org/10.1038/s41612-022-00272-4

Humphrey, V., & Gudmundsson, L. (2019). GRACE-REC: A reconstruction of climate-driven water storage changes over the last century [dataset]. *Earth System Science Data*, *11*(3), 1153–1170. https://doi.org/10.5194/essd-11-1153-2019

IPCC. (2022). In *Global warming of 1.5°C*. Cambridge University Press.

Iturbide, M., Fernández, J., Gutiérrez, J. M., Bedia, J., Cimadevilla, E., Díez-Sierra, J., et al. (2021). Repository supporting the implementation of FAIR principles in the IPCC-WGI Atlas Zenodo [Dataset]. https://zenodo.org/records/5171760

Japan Meteorological Agency/Japan. (2013). JRA-55: Japanese 55-year reanalysis, monthly means andVariances [Dataset]. *Research Data Archive at the National Center for Atmospheric Research, Computational and Information Systems Laboratory*. https://doi.org/10.5065/D60G3H5B. Accessed on 25 03 2022.

Jones, B., & O'Neill, B. C. (2016). Spatially explicit global population scenarios consistent with the Shared Socioeconomic Pathways [Dataset]. *Environmental Research Letters*, *11*(8). https://doi.org/10.1088/1748-9326/11/8/084003.84003.

Jones, B., O'Neill, B. C., McDaniel, L., McGinnis, S., Mearns, L. O., & Tebaldi, C. (2015). Future population exposure to US heat extremes. *Nature Climate Change*, *5*(7), 652–655. https://doi.org/10.1038/NCLIMATE2631

Kephart, J. L., Sánchez, B. N., Moore, J., Schinasi, L. H., Bakhtsiyarava, M., Ju, Y., et al. (2022). City-level impact of extreme temperatures and mortality in Latin America. *Nature Medicine*, *28*(8), 1700–1705. https://doi.org/10.1038/s41591-022-01872-6

Keune, J., Schumacher, D. L., & Miralles, D. G. (2022). A unified framework to estimate the origins of atmospheric moisture and heat using Lagrangian models. *Geoscientific Model Development*, *15*(5), 1875–1898. https://doi.org/10.5194/gmd-15-1875-2022

Kobayashi, S., Ota, Y., Harada, Y., Ebita, A., Moriya, M., Onoda, H., et al. (2015). The JRA-55 reanalysis: General specifications and basic characteristics. *Journal of the Meteorological Society of Japan. Ser. II*, *93*(1), 5–48. https://doi.org/10.2151/jmsj.2015-001

Konapala, G., Mishra, A. K., Wada, Y., & Mann, M. E. (2020). Climate change will affect global water availability through compounding changes in seasonal precipitation and evaporation. *Nature Communications*, *11*(1), 3044. https://doi.org/10.1038/s41467-020-16757-w

Kornhuber, K., Osprey, S., Coumou, D., Petri, S., Petoukhov, V., Rahmstorf, S., & Gray, L. (2019). Extreme weather events in early summer 2018 connected by a recurrent hemispheric wave-7 pattern. *Environmental Research Letters*, *14*(5), 54002. https://doi.org/10.1088/1748-9326/ab13bf

Krueger, O., Hegerl, G. C., & Tett, S. F. B. (2015). Evaluation of mechanisms of hot and cold days in climate models over Central Europe. *Environmental Research Letters*, *10*(1), 14002. https://doi.org/10.1088/1748-9326/10/1/014002

Kunkel, K. E., Changnon, S. A., Reinke, B. C., & Arritt, R. W. (1996). The july 1995 heat wave in the midwest: A climatic perspective and critical weather factors. *Bulletin America Meteorology Social*, *77*(7), 1507–1518. https://doi.org/10.1175/1520-0477(1996)077<1507:TJHWIT>2.0.CO;2

Lange, S. (2019). WFDE5 over land merged with ERA5 over the ocean (W5E5). V. 1.0 [Dataset]. *GFZ Data Services*. https://doi.org/10.5880/pik.2019.023

Laux, P., Rötter, R. P., Webber, H., Dieng, D., Rahimi, J., Wei, J., et al. (2021). To bias correct or not to bias correct? An agricultural impact modelers' perspective on regional climate model data. *Agricultural and Forest Meteorology*, *304–305*, 108406. 304-305. https://doi.org/10.1016/j.agrformet.2021.108406

Luo, M., Wu, S., Liu, Z., & Lau, N.-C. (2022). Contrasting circulation patterns of dry and humid heatwaves over southern China. *Geophysical Research Letters*, *49*(16). https://doi.org/10.1029/2022GL099243

Merrifield, A. L., Brunner, L., Lorenz, R., Humphrey, V., & Knutti, R. (2023). Climate model selection by independence, performance, and spread (ClimSIPS v1.0.1) for regional applications. *Geoscientific Model Development*, *16*(16), 4715–4747. https://doi.org/10.5194/gmd-16-4715-2023

Miralles, D. G., Gentine, P., Seneviratne, S. I., & Teuling, A. J. (2019). Land-atmospheric feedbacks during droughts and heatwaves: State of the science and current challenges. *Annals of the New York Academy of Sciences*, *1436*(1), 19–35. https://doi.org/10.1111/nyas.13912

Miralles, D. G., Teuling, A. J., van Heerwaarden, C. C., & Vilà-Guerau de Arellano, J. (2014). Mega-heatwave temperatures due to combined soil desiccation and atmospheric heat accumulation. *Nature Geoscience*, *7*(5), 345–349. https://doi.org/10.1038/ngeo2141

Mu, M., de Kauwe, M. G., Ukkola, A. M., Pitman, A. J., Guo, W., Hobeichi, S., & Briggs, P. R. (2021). Exploring how groundwater buffers the influence of heatwaves on vegetation function during multi-year droughts. *Earth System Dynamic*, *12*(3), 919–938. https://doi.org/10.5194/esd-12-919-2021

Nairn, J., Ostendorf, B., & Bi, P. (2018). Performance of excess heat factor severity as a global heatwave health impact index. *International Journal of Environmental Research and Public Health*, *15*(11), 2494. https://doi.org/10.3390/ijerph15112494

Ndehedehe, C. E., & Adeyeri, O. E. (2024). Changes in drought characteristics and heatwave propagation over groundwater basins in Australia. *Earth System Environment*. https://doi.org/10.1007/s41748-024-00463-4

Ndehedehe, C. E., Adeyeri, O. E., Onojeghuo, A. O., Ferreira, V. G., Kalu, I., & Okwuashi, O. (2023). Understanding global groundwater-climate interactions. *Science of the Total Environment*, *904*, 166571. https://doi.org/10.1016/j.scitotenv.2023.166571

Ndehedehe, C. E., Ferreira, V. G., Adeyeri, O. E., Correa, F. M., Usman, M., Oussou, F. E., et al. (2023). Global assessment of drought characteristics in the Anthropocene. *Resources, Environment and Sustainability*, *12*, 100105. https://doi.org/10.1016/j.resenv.2022.100105

Nick, J., MzukisiI, G., & Akoon, I. (2022). Beating the heat in South African cities: Lessons from a citizen science assessment. https://blogs.worldbank.org/sustainablecities/beating-heat-south-african-cities-lessons-citizen-science-assessment. accessed 12 December 2023.

NOAA. (2020). Historic july 12-15, 1995 heat wave. Retrieved from https://www.weather.gov/lot/1995_heatwave_anniversary. accessed 10 December 2024.

Pachauri, R. K. & Mayer, L. (Eds.) (2015). *Climate change 2014: Synthesis report longer report [intergovernmental Panel on climate change]; Canadian electronic library, [Geneva, Switzerland]*.

Perkins, S. E., Argüeso, D., & White, C. J. (2015). Relationships between climate variability, soil moisture, and Australian heatwaves. *Journal of Geophysical Research*, *120*(16), 8144–8164. https://doi.org/10.1002/2015JD023592

Perkins-Kirkpatrick, S. E., & Lewis, S. C. (2020). Increasing trends in regional heatwaves. *Nature Communications*, *11*(1), 3357. https://doi.org/10.1038/s41467-020-16970-7

Raymond, C., Matthews, T., & Horton, R. M. (2020). The emergence of heat and humidity too severe for human tolerance. *Science Advances*, *6*(19), eaaw1838. https://doi.org/10.1126/sciadv.aaw1838

R Core Team. (2022). A language and environment for statistical computing. Retrieved from https://www.R-project.org/

Riahi, K., van Vuuren, D. P., Kriegler, E., Edmonds, J., O'Neill, B. C., Fujimori, S., et al. (2017). The Shared Socioeconomic Pathways and their energy, land use, and greenhouse gas emissions implications: An overview. *Global Environmental Change*, *42*, 153–168. https://doi.org/10.1016/j.gloenvcha.2016.05.009

Röthlisberger, M., & Papritz, L. (2023). Quantifying the physical processes leading to atmospheric hot extremes at a global scale. *Nature Geoscience*, *16*(3), 210–216. https://doi.org/10.1038/s41561-023-01126-1

Schär, C. (2016). The worst heat waves to come. *Nature Climate Change*, *6*(2), 128–129. https://doi.org/10.1038/nclimate2864

Schulzweida, U. (2022). CDO user guide; 2022.

Schumacher, D. L., Keune, J., van Heerwaarden, C. C., Vilà-Guerau de Arellano, J., Teuling, A. J., & Miralles, D. G. (2019). Amplification of mega-heatwaves through heat torrents fuelled by upwind drought. *Nature Geoscience*, *12*(9), 712–717. https://doi.org/10.1038/s41561-019-0431-6

Seneviratne, S. I., Corti, T., Davin, E. L., Hirschi, M., Jaeger, E. B., Lehner, I., et al. (2010). Investigating soil moisture–climate interactions in a changing climate: A review. *Earth-Science Reviews*, *99*(3–4), 125–161. https://doi.org/10.1016/j.earscirev.2010.02.004

Shao, L., Liao, W., Li, P., Luo, M., Xiong, X., & Liu, X. (2023). Drivers of global surface urban heat islands: Surface property, climate background, and 2D/3D urban morphologies. *Building and Environment*, *242*, 110581. https://doi.org/10.1016/j.buildenv.2023.110581

Strobl, C., Boulesteix, A.-L., Kneib, T., Augustin, T., & Zeileis, A. (2008). Conditional variable importance for random forests. *BMC Bioinformatics*, *9*(1), 307. https://doi.org/10.1186/1471-2105-9-307

Taguela, T. N., Akinsanola, A. A., Bobde, V., Raji, I., Adeyeri, O. E., & Adebiyi, A. A. (2025). Precipitation distribution over Africa: Observations and modeling. In *Aerosols and precipitation over Africa* (pp. 121–146). Elsevier.

Trenberth, K. E., Fasullo, J. T., & Kiehl, J. (2009). Earth's global energy budget. *Bulletin America Meteorology Social*, *90*(3), 311–324. https://doi.org/10.1175/2008BAMS2634.1

Tripathy, K. P., Mukherjee, S., Mishra, A. K., Mann, M. E., & Williams, A. P. (2023). Climate change will accelerate the high-end risk of compound drought and heatwave events. *Proceedings of the National Academy of Sciences*, *120*(28). https://doi.org/10.1073/pnas.2219825120

Ullah, S., You, Q., Ullah, W., Sachindra, D. A., Ali, A., Bhatti, A. S., & Ali, G. (2023). Climate change will exacerbate population exposure to future heat waves in the China-Pakistan economic corridor. *Weather and Climate Extremes*, *40*, 100570. https://doi.org/10.1016/j.wace.2023.100570

Usman, M., Manzanas, R., Ndehedehe, C. E., Ahmad, B., Adeyeri, O. E., & Dudzai, C. (2022). On the benefits of bias correction techniques for streamflow simulation in complex terrain catchments: A case-study for the Chitral river basin in Pakistan. *Hydrology*, *9*(11), 188. https://doi.org/10.3390/hydrology9110188

Vitali, A., Felici, A., Esposito, S., Bernabucci, U., Bertocchi, L., Maresca, C., et al. (2015). The effect of heat waves on dairy cow mortality. *Journal of Dairy Science*, *98*(7), 4572–4579. https://doi.org/10.3168/jds.2015-9331

Vogel, M. M., Zscheischler, J., Fischer, E. M., & Seneviratne, S. I. (2020). Development of future heatwaves for different hazard thresholds. *Journal of Geophysical Research: Atmospheres*, *125*(9), e2019JD032070. https://doi.org/10.1029/2019JD032070

Vogel, M. M., Zscheischler, J., Wartenburger, R., Dee, D., & Seneviratne, S. I. (2019). Concurrent 2018 hot extremes across northern hemisphere due to human-induced climate change. *Earth's Future*, *7*(7), 692–703. https://doi.org/10.1029/2019EF001189

Wang, P., Zhang, Q., Yang, Y., & Tang, J. (2019). The sensitivity to initial soil moisture for three severe cases of heat waves over eastern China. *Frontiers in Environmental Science*, *7*. https://doi.org/10.3389/fenvs.2019.00018

Wang, X., Zhang, Z., Yu, E., Guo, C., Otterå, O. H., & Counillon, F. (2024). Warm advection as a cause for extreme heat event in North China. *Geophysical Research Letters*, *51*(12). https://doi.org/10.1029/2024GL108995

Wang, Y., Zhao, N., Wu, C., Quan, J., & Chen, M. (2023). Future population exposure to heatwaves in 83 global megacities. *Science of the Total Environment*, *888*, 164142. https://doi.org/10.1016/j.scitotenv.2023.164142

Wang, Z.-H., Wang, C., & Yang, X. (2021). Dynamic synchronization of extreme heat in complex climate networks in the contiguous United States. *Urban Climate*, *38*, 100909. https://doi.org/10.1016/j.uclim.2021.100909

Weedon, G. P., Balsamo, G., Bellouin, N., Gomes, S., Best, M. J., & Viterbo, P. (2014). The WFDEI meteorological forcing data set: WATCH forcing data methodology applied to ERA-interim reanalysis data. *Water Resources Research*, *50*(9), 7505–7514. https://doi.org/10.1002/2014WR015638

Xiao, H., Xu, P., & Wang, L. (2024). The unprecedented 2023 north China heatwaves and their S2S predictability. *Geophysical Research Letters*, *51*(6). https://doi.org/10.1029/2023GL107642

Xu, Z., FitzGerald, G., Guo, Y., Jalaludin, B., & Tong, S. (2016). Impact of heatwave on mortality under different heatwave definitions: A systematic review and meta-analysis. *Environment International*, *89–90*, 193–203. https://doi.org/10.1016/j.envint.2016.02.007

Yu, B., Lin, H., Mo, R., & Li, G. (2023). A physical analysis of summertime North American heatwaves. *Climate Dynamics*, *61*(3–4), 1551–1565. https://doi.org/10.1007/s00382-022-06642-1

Zhao, M., A, G., Velicogna, I., & Kimball, J. S. (2017). Satellite observations of regional drought severity in the continental United States using GRACE-based terrestrial water storage changes. *Journal of Climate*, *30*(16), 6297–6308. https://doi.org/10.1175/JCLI-D-16-0458.1

Zipper, S. C., Keune, J., & Kollet, S. J. (2019). Land use change impacts on European heat and drought: Remote land-atmosphere feedbacks mitigated locally by shallow groundwater. *Environmental Research Letters*, *14*(4), 44012. https://doi.org/10.1088/1748-9326/ab0db3

Zscheischler, J., Michalak, A. M., Schwalm, C., Mahecha, M. D., Huntzinger, D. N., Reichstein, M., et al. (2014). Impact of large-scale climate extremes on biospheric carbon fluxes: An intercomparison based on MsTMIP data. *Global Biogeochemical Cycles*, *28*(6), 585–600. https://doi.org/10.1002/2014GB004826

Zschenderlein, P., Fink, A. H., Pfahl, S., & Wernli, H. (2019). Processes determining heat waves across different European climates. *Quarterly Journal of the Royal Meteorological Society*, *145*(724), 2973–2989. https://doi.org/10.1002/qj.3599